

1 **Quantitative Study of Storm Surge Risk Assessment in Undeveloped Coastal Area of China**
2 **Based on Deep Learning and Geographic Information System (GIS) Techniques: A Case**
3 **Study of Double-Moon Bay Zone**

4 Lichen Yu ^{a, d}, [Shining Huang^c](#), Hao Qin ^{*, a, d}, [Shining Huang^c](#), Wei Wei ^{a, d}, [Haoyu Jiang^{a, d}](#), Lin
5 Mu ^{*, b}

6 ^a Hubei Key Laboratory of Marine Geological Resources, College of Marine Science and
7 Technology, China University of Geosciences, Wuhan, China, 430074

8 ^b College of Life Sciences and Oceanography, Shenzhen University, Shenzhen, China, 518060

9 ^c Marine Information Center, Department of Natural Resources of Huizhou Bureau, Huizhou,
10 China, 516003

11 ^d Shenzhen Research Institute, China University of Geosciences, Shenzhen, China, 518057

12
13 * Corresponding authors: Hao Qin (qh1qh100@alumni.sjtu.edu.cn); Lin Mu (moulin1977@hotmail
14 l.com).

15
16 **Abstract**

17 Storm surge is a common nature disaster in China southern coastal area, which usually causes
18 heavy human life and economic losses. With the economic development and population
19 concentration of coastal cities, the storm surges may result in more impacts and damage in the
20 future. Therefore, it is of vital importance to conduct risk assessment to identify high-risk areas
21 and evaluate economic losses. However, quantitative study of storm surge risk assessment in
22 undeveloped areas of China is difficult, since there is a lack of building characters and damage
23 assessment data. Aiming at the problem of data missing in undeveloped areas of China, this paper
24 proposes a methodology for conducting storm surge risk assessment quantitatively based on deep
25 learning and geographic information system (GIS) techniques. Five defined storm surge
26 inundation scenarios with different typhoon return periods are simulated by coupled FVCOM-
27 SWAN model, the reliability of which is validated using official measurements. Building
28 footprints of the study area are extracted through TransUNet deep learning model and Remote
29 Sensing Image (RSI), while building heights are obtained through Unmanned Aerial Vehicle (UAV)
30 measurement. Subsequently, economic losses are quantitatively calculated by combing the
31 adjusted depth-damage functions and overlay analysis of the buildings exposed to storm surge
32 inundation. Zonation maps of the study area are illustrated to display the risk levels according to
33 the economic losses. The quantitative risk assessment and zonation maps can help the government
34 to make storm surge disaster prevention measures and optimize land use planning, and thus to
35 reduce the potential economic losses of the coastal area.

36
37 **Keywords:** Storm surge; Quantitative risk assessment; GIS; Deep learning; Risk zonation map

38
39 **1. Introduction**

40 Storm surge, defined as the abnormal rise of water over and above the normal astronomical
41 tide, and is expressed in terms of height above predicted or expected tide levels. Mostly, the surge
42 is generated by a strong atmospheric disturbance, and it becomes particularly catastrophic when it
43 happens to coincide with an astronomical high tide. In that case, the surge-driven coastal flooding
44 may inundate buildings and cropland, cause significant casualties and economic losses. Storm

45 surges have caused widespread damage worldwide. In 2013, super typhoon Yolanda as the worst
46 typhoon in last 30 years, pounded the Philippines. It caused 6293 individuals reported dead, 28689
47 injuries and 1061 individuals missing, with estimated damages totaling 864 million US dollars
48 (Mcperson, 2015). Hurricane Harvey struck Texas in August 2017, resulting in approximately
49 100 deaths and economic losses exceeding 125 billion dollars (Lee, 2021). In China, storm surges
50 also pose a frequent threat in the coastal cities. In the last decade, China has experienced an
51 average of 8.5 storm surge disasters annually, with an average damage amount of 6815.8 million
52 yuan per year, where Guangdong and Zhejiang Provinces are the most affected coastal areas
53 (China Marine disaster bulletin, 2022). For example, Typhoon Hato in 2017, Typhoon Mangkhut
54 in 2018, Typhoon Lekima in 2019 has caused significant damage to coastal cities in China, and
55 resulted great losses of life and property (Zhou et al., 2021; Yang et al., 2019)~~For example,~~
56 ~~Typhoon Hato in 2017, Typhoon Mangkhut in 2018, Typhoon Lekima in 2019 has caused~~
57 ~~significant damage to coastal cities in China, and resulted great losses of life and property.~~ For the
58 past few years, as the rapid development of population and economic in China coastal area, the
59 potential monetary loss grows accordingly (Fang et al., 2021; Ji et al., 2020; Mcgranahan et al.,
60 2007; Seto et al., 2011). Therefore, it is crucial to implement risk assessment and mapping
61 strategies to effectively reduce these risks and mitigate the impact of storm surges.

62 Storm surge hazard assessment is an essential component of storm surge risk assessment and
63 zoning, aiming to evaluate the hazard intensity of disasters, through numerical simulation of storm
64 surge processes, estimation of storm surge for selected return periods, and computation of the
65 probable maximum storm surge (Shi et al., 2013). Therefore, the numerical simulation of storm
66 surge is a key step for storm surge risk assessment. ~~However, B~~because of the limitation of
67 historical storms and the nondeterminacy of future storm, numerical simulation of storm surges is
68 usually used to determine storm levels. Hydrodynamic model such as Advanced Circulation Mode
69 (ADCIRC), Delft3D and Finite Volume Coastal Ocean Model (FVCOM) have been widely used
70 (Vijayan et al., 2021; Wang et al., 2021a; Liu and Huang, 2020; Hu et al., 2022; Lyddon et al.,
71 2019; Zhang et al., 2020; Zhu et al., 2022).~~Advanced Circulation Mode (ADCIRC) is a widely~~
72 ~~used hydrodynamic model in coastal area. For example, Vijayan et al. (2021) utilized ADCIRC~~
73 ~~model to simulate storm surges and tides during the hurricane that land on Florida in 2018, for the~~
74 ~~purpose of comparing the different impact of wind model Holland 1980 and Holland 2010. Wang~~
75 ~~et al. (2021a) and Liu and Huang (2020) used ADCIRC and Simulating Waves Nearshore (SWAN)~~
76 ~~coupled model respectively simulate the storm surge and wave in the sea near Shandong Peninsula~~
77 ~~and Taiwan, and the hazard assessment and model verification were carried out respectively.~~
78 ~~Delft3D is a comprehensive numerical modeling system for simulating hydrodynamic processes.~~
79 ~~Hu et al. (2022) adapted a pre-validated Delft3D-based hydrodynamic model proved the impact of~~
80 ~~levee opening at selected locations was minor. Lyddon et al. (2019) used Delft3D FLOW WAVE~~
81 ~~model calculate the tide and wave in the Severn Estuary, the result pointed out the importance of~~
82 ~~locally generating winds in simulation of water level and wave height. Finite Volume Coastal~~
83 ~~Ocean Model (FVCOM) is another widely used numerical model for simulating hydrodynamic~~
84 ~~processes. Zhang et al. (2020) conducted a series of modeling experiments with the purpose of~~
85 ~~assessing the impact of storm and evaluated the flood protection by using FVCOM inundation~~
86 ~~model. Zhu et al. (2022) realized WRF-SWAN-FVCOM coupling simulation to analyze the~~
87 ~~spatial-temporal evolution laws, and the result demonstrate the method can predict hydroelastic~~
88 ~~responses of the maritime airport under the impact of typhoons, currents and waves.~~

89 It has been demonstrated that it is critical to include tide and sea-water-level variations in shelf and
90 nearshore wave simulations (Masson, 1996). Furthermore, the sea water level could be
91 significantly affected by strong tide and typhoon-induced wind in complex coastal seas and then
92 modulate the wave properties (Yang et al., 2020). Coupled FVCOM-SWAN model, with the
93 foundation of FVCOM's finite volume method, unstructured grid, and adaptable boundary
94 condition handling capability, integrating the hydrodynamic and wave processes of SWAN,
95 possesses the ability to provide simulation result more quickly and accurately. In this circumstance,
96 coupled FVCOM-SWAN model is used in this research for simulating the inundation of storm
97 surge.

98 Coastal risk assessment can be categorized into two primary classifications: qualitative and
99 quantitative. In the realm of qualitative assessment, entropy weight method, Analytic Hierarchy
100 Process (AHP) and other methods are widely used. Ramkar and Yadav (2021) used AHP in
101 combination with Geographic Information Systems (GIS) for proposing a flood risk map, which
102 can identify the high-risk areas efficiently. Malekinezhad et al. (2021) combined the entropy
103 weight method and GIS, and conducted a flood vulnerability analysis for Hamadan city. The
104 results highlighted the advantages of entropy weight method comparing to normal spatial overlay
105 method. Besides, Pathan et al. (2022) and Rafiei-Sardooi et al. (2021) made use of Technique for
106 Order Preference of Similarity by Ideal Solution (TOPSIS). The former pointed out the
107 advancement of TOPSIS by comparing with AHP, and the latter combined machine learning and
108 TOPSIS to analyze urban flood vulnerability. Unlike qualitative risk assessment, quantitative risk
109 assessment enables the quantification of damages and risks in monetary terms. The most
110 commonly used approach to assess direct damages is based on depth-damage curves (De Moel and
111 Aerts, 2011; Merz et al., 2007; Smith, 1994). Thielen et al. (2008) presented the Flood Loss
112 Estimation Model for the private sector (FLEMOPs) through using the Germany flood losses data
113 in August 2002, and the group further established model for commercial sector in 2010 (Kreibich
114 et al., 2010). Zhai et al. (2005) derived multi-factor loss functions for buildings in Nagoya, Japan
115 using empirical data from Tokai flood in 2000, and Grahn and Nyberg (2014) established
116 functional relationships utilizing the house insurance claims data caused by lake flooding. Except
117 for buildings, Yazdi and Salehi Neyshabouri (2012) and Hess and Morris (1988) respectively built
118 several uni-variable functions and multi-factor functions for kinds of crops and grassland. In
119 recent years, machine learning is also introduced in quantitative loss assessment, for example,
120 Merz et al. (2013) developed a tree-based approach using Regression Tree and Bagging
121 Regression Tree as machine-learning methods to analysis of direct building damage to private
122 homes. Paprotny et al. (2020) proposed a Bayesian Network damage model (a ~~Supervised-~~
123 ~~Machine-Learning-learning~~ method), and reached a good accuracy of predictions of
124 building losses.

125 The essence of quantitative risk assessment lies in analyzing the interaction between
126 exposure factors and hazards (Adnan et al., 2020; Armenakis and Nirupama, 2013; Granger, 2003;
127 Kron, 2005). Therefore it's crucial to quantify the direct tangible damage of elements at risk.
128 Buildings are important exposure elements, as they are the gathering place of population and
129 property. Building footprint data is necessary for evaluating the vulnerabilities of a building, as it
130 provides essential information about the buildings, including spatial location, distribution, and
131 boundaries and so on (Mharzi Alaoui et al., 2022). It's also of great significance in risk assessment,
132 primarily due to its ability to identify high-risk areas, assess building vulnerability and estimate

133 potential damage (Gacu et al., 2023; Wu et al., 2019). Extracting building footprints from remote
134 sensing images has been widely used in many fields, such as urban management, disaster
135 management, navigation (Zhou et al., 2004; Tang et al., 2006; Liu et al., 2019; Liu et al., 2020;
136 Rousell and Zipf, 2017; Chen and Gao, 2019). However, there is a lack of building footprints
137 extraction and application in the realm of storm surge assessment. -

138 When the building is inundated, there are a variety of factors that may influence the amount
139 of monetary loss. For example, building type, building structure, private precaution, maintenance
140 status, and others (Marvi, 2020; Thieken et al., 2008). Taramelli et al. (2022) pointed out that
141 building's height is one of the factors for determining the susceptibility due to flooding and
142 evaluate the buildings' potential damage by flood hazards. Hasanzadeh Nafari et al. (2016)
143 developed a new loss model, in which building with different story were divided into different
144 categories in the modelling process. To conclude, height is an important factor that affecting the
145 vulnerability of buildings when they serve as inundation-exposed elements. Therefore, in the
146 process of quantitative storm surge risk assessment, it is necessary to adjust the depth-damage
147 functions to make buildings of different heights correspond to different functions.

148 Besides, different from the field research and statistics required for other data acquisition, the
149 data of buildings' height is more accessible from multiple sources. For example, public data DSM
150 data has been utilized for building height estimation (Huang et al., 2022), some satellite companies
151 also offer services to customize DSM data for selected regions. Nonetheless, they respectively
152 suffer from a lack of precision and high costs. Building height can also be obtained via remote
153 sensing technique, such as Synthetic Aperture Radar (SAR) (Li et al., 2020; Frantz et al., 2021), or
154 take advantage of shadow in remote sensing images (Comber et al., 2011; Shao et al., 2011).
155 However, in addition to the lack of precision, the absence of data necessary for modelling and the
156 crowded character of rural buildings in China make the above methods difficult to be implemented.
157 Compared to methods above, acquiring building height through UAV ensures high accuracy while
158 being relatively efficient, and the method is quite simple, which also reduces the required costs.

159 For example, in urban planning, Zhou et al. (2004) used building footprint data and LiDAR
160 point cloud data for urban 3D modeling; Tang et al. (2006) proposed a GIS-based landscape index
161 combing with remote sensing to analyze urban sprawl spatial fragmentation. In disaster
162 management, Liu et al. respectively evaluated seismic vulnerability in Urumqi and Weinan in
163 China (Liu et al., 2019; Liu et al., 2020). In navigation, Rousell and Zipf (2017) proposed a
164 prototype navigation service based on multi-index in OSM dataset and building footprints, and
165 Chen and Gao (2019) merged GPS pseudorange, LiDAR odometry measurements and building
166 footprint to offer a UAV navigation algorithms. However, there is a lack of building footprints
167 extraction and application in the realm of storm surge assessment.

168 In view of the aforementioned information, regarding storm surge qualitative risk assessment,
169 there is a stringent requirement for both the quality and timeliness of land use data, which means
170 that the risk assessment cannot be generated in real time, and the qualitative risk assessment also
171 can't evaluate the risk level through the intuitive value of economic loss. In the realm of
172 quantitative risk assessment, building a uni-variable or multi-factor empirical model requires
173 complete and substantial data, and the published models generally only provide uni-variable
174 functions ignoring the building height as a factor, or have regional limitations. Additionally, for
175 the coastal regions of China, which are often affected by storm surge disasters, they tend to have
176 relatively low levels of economic development. Under the circumstances, the data needed to

177 conduct flood risk assessment is generally in a state of absence.

178 In response to the challenges mentioned above, the scientific goal of this paper is to propose a
179 quantitative storm surge risk assessment method for underdeveloped areas based on deep learning
180 and GIS techniques. First, on the basis of high-resolution DEM and seawall data measurement,
181 five defined storm surge inundation scenarios with different typhoon return periods are simulated
182 by employing the coupled FVCOM-SWAN model. Subsequently, TransUNet is introduced as a
183 deep learning method to extract building footprint, and building's height data is acquired through
184 UAV measurement. Since data on relevant disaster losses in underdeveloped regions are lacking,
185 empirical modeling was deemed impractical. Therefore, the adjustment of the JRC's depth-
186 damage curves by the HAZUS is chosen to take the impact building's height into consideration,
187 thus to conduct a quantitative assessment with more accuracy. Finally, combining hazard map,
188 exposure elements and adjusted depth-damage curves, the quantitative risk zoning maps are
189 conducted. The risk zoning maps can assist decision-makers in identifying high-risk sub-zones and
190 planning disaster prevention measures. Accordingly, the novelty can be seen in obtaining refined
191 exposure elements data through deep learning and UAV, addressing the lack of historical storm
192 surge economic loss data and considering the effect of building height on economic loss through
193 the adjustment of existing depth-damage curves.

194 **2. Study area and datasets**

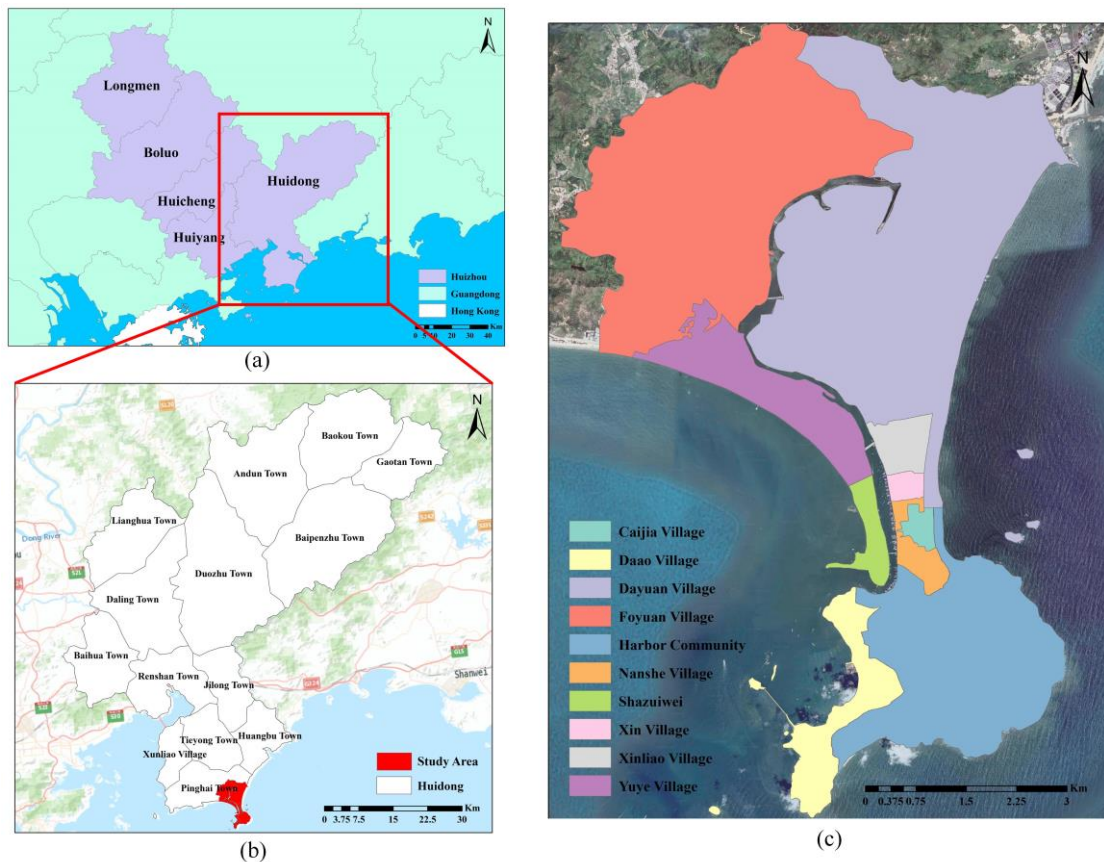
195 *2.1. Study area*

196 Being the shipping hub in the South China Sea, Guangdong province, located in southern
197 China, has become the largest economic province in China since 1989, with a GDP of 129118.6
198 billion yuan in 2022. Due to the seaborne trade, Guangdong has been the largest economic
199 province in China since 1989, which reached a GDP of 129118.6 billion yuan in 2022. However,
200 just as mentioned above, Guangdong is relatively vulnerable to storm surges, such as Typhoon
201 Hato and Typhoon Mangkhut, due to its geographical characteristics.~~However, just as mentioned~~
202 ~~above, Guangdong is relatively vulnerable to storm surges because of its geographical~~
203 ~~characteristics, such as Typhoon Hato and Typhoon Mangkhut.~~

204 Huizhou is one of the cities in Guangdong province, and also one of the central cities of Pearl
205 River Delta region. It's located at on the east coast of Guangdong-Hong Kong-Macao Greater Bay
206 Area, the GDP reached 540.1 billion yuan in 2022, with the highest growth rate in Guangdong.
207 Pinghai Town located at the southernmost of Huizhou, and has a registered population of about
208 forty thousand. Its economic source mainly depends on various crops and seafood products. Due
209 to its coastal geographical characteristics and the presence of Pinghai Ancient City, the town has
210 become a cultural tourist destination and can therefore be defined as a cultural tourist town.

211 In this paper, the chosen study region is the coastal area of Pinghai town, named the Double-
212 Moon Bay Zone. It covers ten villages in total, including Foyuan, Dayuan, Yuye, Xinliao, Xin
213 village, Shazuiwei, Cajia, Nanshe, Daa, and Harbor community. These years, the region has been
214 developed in tourism and real estate project development including construction of hotels, resorts,
215 and high-end business districts, which vastly prompt the financial development. It is foreseeable
216 that the population and economy of the region will growth rapidly. However, the economic status
217 of the region remains relatively low, which presents a challenge due to data scarcity and limited
218 accessibility~~However, the region's general economic status, which remains relatively low, and it~~
219 ~~consequently gives rise to the challenge of data scarcity and limited accessibility.~~ In addition, the
220 region is susceptibly affected by the tropical cyclones during the season running from April to

221 November (Wang et al., 2021b). Recent years, more than ten typhoons have affected the study
222 area, including Typhoon Lekima, Typhoon Haishen, Typhoon Kanuni etc. The general location
223 and information about the study area is shown on Fig. 1.



224

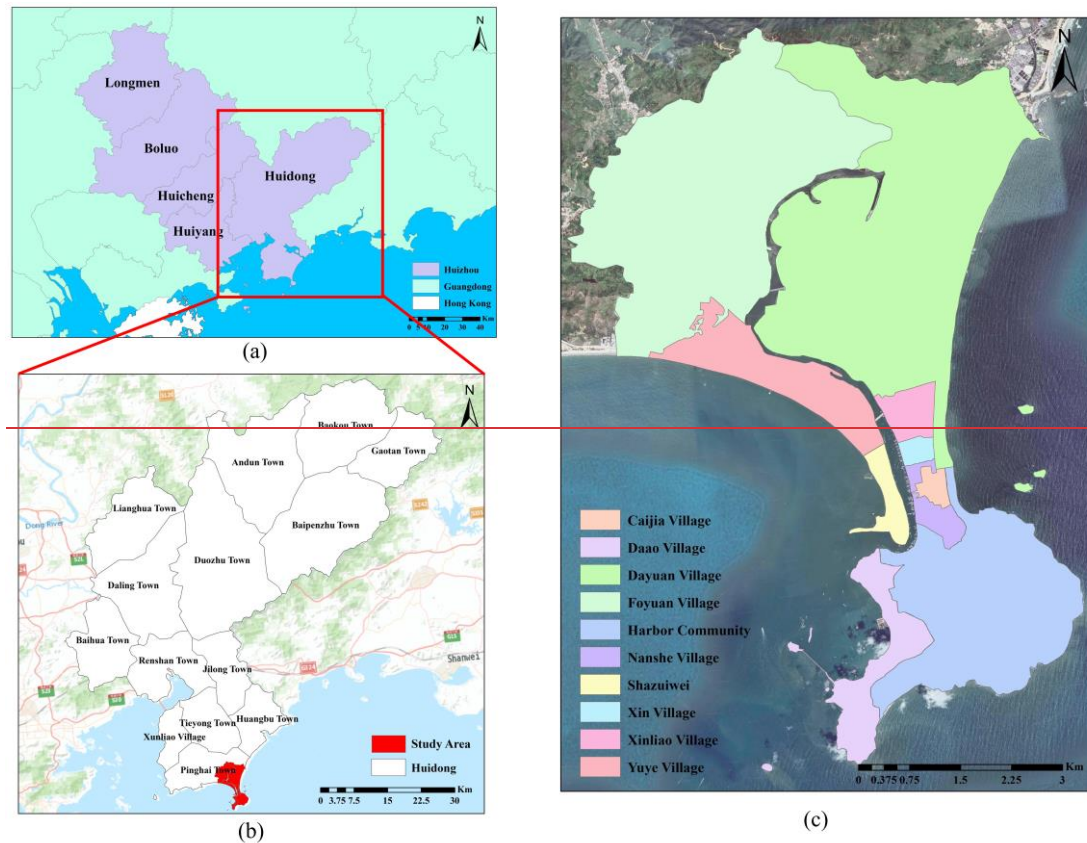


Fig. 1. The maps of locations in the study: (a) The map of Huizhou; (b) The map of study area in Huidong, the base map is obtained from ESRI; (c) The village map of study area, the base map is obtained from © GoogleMaps (map data © 2023 Google).

2.2. Data source

In order to accomplish the research, the data used is obtained from various sources, here is the describe of different data:

(1) Land Cover Types data: the data is obtained from the Department of Natural Resources of Huizhou Bureau. It contains multiple land cover types including forest, cropland, residential land, etc. It is used to calculate vulnerability level.

(2) Remote sensing images: the remote sensing images are obtained from Chang Guang Jilin-1 satellite. Chang Guang Satellite technology CO., LTD was founded on December 1st 2014, which is the first and the largest commercial satellite corporation in China. Jilin-1 is the first self-developed commercial high-resolution satellite. The images from Jilin-1 satellite have a resolution of 50 cm, and have five spectral channels: Panchromatic band; Blue band; Red band; Green band; Near Infrared band. The images consisting of blue band, red band, green band are utilized to combine deep learning method, thus achieve the extraction of buildings.

(3) Unmanned Aerial Vehicle (UAV) data: the UAV data is generated by oblique photography, and is organized by Open Scene Graph Binary format. The UAV data is obtained from Department of Natural Resources of Huizhou Bureau, and the data is utilized for buildings' height calculation.

(4) Digital elevation model (DEM) data: the DEM data is captured by manual observation in 2018, with the resolution of 0.3m. The coordinate system and file organization are originally CGCS 2000 and txt file, and further transformed to WGS 1984 and raster format to make use of

249 these data in the research. The data contains the elevation information for the study region.
250 Besides, the seawall data is also obtained manually. Both data are used in modeling of storm
251 surges for simulating the hazard maps.

252 (5) Hybrid wind field: ERA5 is the fifth generation of the European Reanalysis dataset
253 produced by the European Centre for Medium-Range Weather Forecasts (ECMWF), and it
254 provides the comprehensive and high-resolution atmospheric and climate data. Holland typhoon
255 wind field model was proposed by Holland in 1980, which introduced Holland B parameter on the
256 basis of the Schloemer exponential pressure distribution model (Holland, 1980). In this study, the
257 two data are fused to generate hybrid wind field data, which is subsequently utilized for storm
258 surge simulations. ~~(5) ERA5 data: ERA5 is the fifth generation of the European Reanalysis dataset~~
259 ~~produced by the European Centre for Medium Range Weather Forecasts (ECMWF), and it~~
260 ~~provides the comprehensive and high-resolution atmospheric and climate data. In this study, the~~
261 ~~data is used in conjunction with the Holland method to generate fused wind field data, which is~~
262 ~~subsequently utilized for storm surge simulations.~~

263 (6) Historical typhoon data: the historical typhoon data including typhoon track, typhoon
264 pressure, and velocity are obtained through China Meteorological Administration Typhoon
265 Network Website. The historical data is employed to assess the reliability and validity of the
266 model.

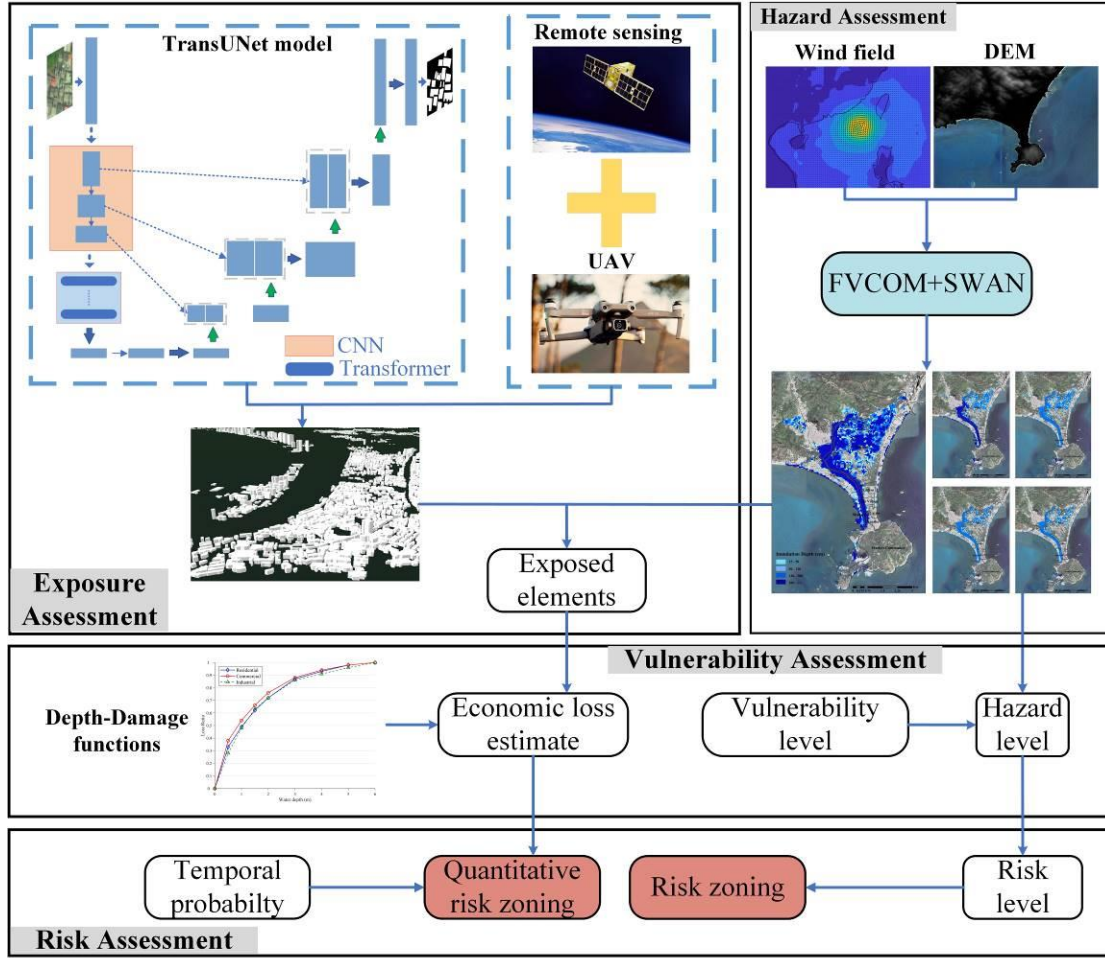
267 (7) Administrative Boundary data: the data is obtained from National Platform for Common
268 Geospatial Information Services, and it contains administrative boundaries at village level~~the data~~
269 ~~is obtained from National geographic information public service platform, and it contains~~
270 ~~administrative boundaries at village level.~~ There are ten villages in the study area.

271

272 **3. Method**

273 The methods in this study aim to assess quantitative direct tangible damage over the study
274 area consists of following steps: hazard assessment; exposure assessment; vulnerability
275 assessment; risk assessment, and the flowchart of the procedure is illustrated in Fig. 2.

276 First, with respect to hazard assessment, five storm surge scenarios are defined. After
277 constructing wind field through Holland model, the inundation area and depth of different typhoon
278 return periods are simulated by utilizing the coupled FVCOM-SWAN model. In exposure
279 assessment, building footprints and heights are extracted by introducing a deep learning method
280 TransUNet and shadow calculation. Then the hazard maps are overlaid to identify the elements at
281 risk. Considering the effect of building's floor in flood monetary loss estimation, the JRC's depth-
282 damage functions are adapted representing the vulnerability of different exposed elements.
283 Eventually, the economic loss of different typhoon scenarios can be summarized and the risk
284 assessment is conducted through multiplying the temporal probability. Moreover, the quantitative
285 zoning maps of four risk levels are generated through zonal statistic.



286

287 **Fig. 2.** The flowchart of the presented storm surge quantitative risk assessment method. The base
 288 map is obtained from © GoogleMaps (map data © 2023 Google).

289

290 *3.1. Storm surge inundation simulation*

291 Finite Volume Coastal Ocean Model (FVCOM), is a coastal ocean circulation model, which
 292 was originally developed by Chen et al. (2003), and further improved by the University of
 293 Massachusetts and the Woods Hole Oceanographic Institution. The following are the governing
 294 equations of FVCOM, comprising momentum, continuity, temperature, salinity, and density
 295 equations:

$$\frac{\partial u}{\partial t} + u \frac{\partial u}{\partial x} + v \frac{\partial u}{\partial y} + w \frac{\partial u}{\partial z} = -\frac{1}{\rho_o} \frac{\partial P}{\partial x} + \frac{\partial}{\partial z} \left(K_m \frac{\partial u}{\partial z} \right) + F_u \quad (3.1)$$

$$\frac{\partial v}{\partial t} + u \frac{\partial v}{\partial x} + v \frac{\partial v}{\partial y} + w \frac{\partial v}{\partial z} + fu = -\frac{1}{\rho_o} \frac{\partial P}{\partial y} + \frac{\partial}{\partial z} \left(K_m \frac{\partial v}{\partial z} \right) + F_v \quad (3.2)$$

$$\frac{\partial P}{\partial z} = -\rho g \quad (3.3)$$

$$\frac{\partial u}{\partial x} + \frac{\partial v}{\partial y} + \frac{\partial w}{\partial z} = 0 \quad (3.4)$$

$$\frac{\partial T}{\partial t} + u \frac{\partial T}{\partial x} + v \frac{\partial T}{\partial y} + w \frac{\partial T}{\partial z} = \frac{\partial}{\partial z} \left(K_h \frac{\partial T}{\partial z} \right) + F_T \quad (3.5)$$

$$\frac{\partial S}{\partial t} + u \frac{\partial S}{\partial x} + v \frac{\partial S}{\partial y} + w \frac{\partial S}{\partial z} = \frac{\partial}{\partial z} \left(K_h \frac{\partial S}{\partial z} \right) + F_S \quad (3.6)$$

$$\rho = \rho(T, S) \quad (3.7)$$

296 Where x , y and z respectively represent the east, north and vertical coordinate axes in the
 297 Cartesian coordinate system; u , v and w are the velocity components in x , y , z directions; T ,
 298 S and ρ are the temperature, salinity and density; P is the pressure and f stands for the
 299 Coriolis parameter; K_m is the vertical eddy viscosity coefficient and K_h is the vertical eddy
 300 diffusivity coefficient for heat; g is the gravitational acceleration; F_u , F_v , F_T , and F_S are the
 301 horizontal diffusion terms.

302 Simulating Waves Nearshore (SWAN) is the third-generation offshore wave model developed
 303 by Delft University of Technology and it was originally proposed by Booij et al. (1996). The
 304 governing equation of the model is shown as

$$\frac{\partial}{\partial t} N + \frac{\partial}{\partial x} C_x N + \frac{\partial}{\partial y} C_y N + \frac{\partial}{\partial \gamma} C_\gamma N + \frac{\partial}{\partial \theta} C_\theta N = \frac{S}{\gamma} \quad (3.8)$$

305 Where N is the wave action density; θ is the propagation direction; C_x , C_y are respectively
 306 the x , y components of propagation speed and C_γ , C_θ are the γ , θ components of propagation
 307 cospeed; γ and S respectively represent the frequency and the source term for the wave energy.

308 The potential storm surge inundation maps in different typhoon scenarios have been
 309 conducted by institutions such as the National Oceanic and Atmospheric Administration (NOAA),
 310 National Hurricane Center, and other departments since the 1990s (Glahn et al., 2009). In the field
 311 of risk assessment research, it is common to set up different typhoon scenarios using storm surge
 312 simulation models to obtain various scenarios of typhoon induced inundation (Zhang et al., 2023;
 313 Rizzi et al., 2017). The hazard maps of under various typhoon intensity scenarios are helpful for
 314 decision-makers and researchers in analysing multiple aspects of potential hazards in the study
 315 area.

316 Typhoon Mangkhut, as one of the largest typhoons to affect South China Sea region in recent
 317 years, has a strong representative. It is characterised by high intensity, wide area of influence, high
 318 wind speed, etc. In this study, the path of Typhoon Mangkhut is shifted to pass through the
 319 Huizhou tidal station as the input typhoon path of the coupled model to maximize the impact area
 320 of the simulation result. In terms of the center pressure, Wang et al. (2021b) presented statistical
 321 analyses of historical typhoon data in Huizhou, and designed five typhoon scenarios, which are
 322 respectively the typhoon minimum central pressure of 880, 910, 920, 930 and 940 hPa. Therefore,
 323 these five parameters are introduced as the setup for five typhoon scenarios.

324 FVCOM and SWAN both use the unstructured triangular grid to subdivide the South China
 325 Sea, and the latitude and longitude range of the region is 13°N - 29°N, 109°E-122°E. The SWAN
 326 parameters are set as follows: wind input growth term and whitecap dissipation term are the
 327 Komen scheme; Bottom friction dissipation is parameterized using the Madsen vortex viscosity
 328 model; The nonlinear interactions are implemented using three-wave and four-wave nonlinear
 329 interaction schemes. The input wind field is the fusing wind field derived from ERA5 and the
 330 Holland method. The open boundary forced tidal elevation of FVCOM is conducted by calculating
 331 the harmonic constants for the eleven major astronomical tidal constituents, namely M2, N2, S2,
 332 K2, K1, O1, P1, Q1, MS4, M4, and M6. The forcing field is the fusing wind field and the wave
 333 data generated by SWAN. The external model time step for the model is set to 0.75 second, while
 334 the internal model time step is set to 7 seconds.

In ~~the present study~~summary, FVCOM-SWAN coupling method is utilized for simulating the inundation caused by storm surge. Specifically, following the modification of typhoon Mangkhut's central pressure, velocity, and track data, the data is utilized as input for the Holland typhoon wind field model, subsequently yielding the wind field outcome. The hybrid wind field data ~~extracted~~ generated is fed into the SWAN model to generate wave data. Then, both the wind data and wave data are input into the FVCOM model to calculate the extent of inundation.

3.2. Buildings extraction

The deep learning model used in the research is TransUNet (Chen et al., 2021), which was originally proposed for medical images segmentation. TransUNet incorporates transformer in encoder within the architecture of U-shape network, consequently makes use of the advantage of global information extraction while fusing the superficial and deep features. On the mission of building extraction, the target is to segment the building's area precisely. The TransUNet model can effectively identify the boundary between buildings and background, which enables the model to be competent for extracting the buildings in different size and shape.

The following is relevant introduction of the structure of the model.

3.2.1. Transformer in TransUNet

Transformer was first proposed by Sutskever et al. (2014), which was originally utilized for machine translation. However, as more variants of transform were developed, people found transform also perform well in multiple tasks, such as natural language processing (NLP), computer vision (CV) and automatic speech recognition (ASR).

The transformer encoder is composed of L layers of Multi-head Self-Attention (MSA), Layer normalization (LN) and Multi-Layer Perceptron (MLP), the structure is shown in the Fig. 3(a), and the equations of Query-Key-Value (QKV) self-attention and MSA are shown below:

$$\text{Attention}(Q, K, V) = \text{softmax}\left(\frac{QK^T}{\sqrt{D_k}}\right)V \quad (3.9)$$

$$\text{MultiHeadAttn}(Q, K, V) = \text{Concat}(\text{head}_1, \dots, \text{head}_H) \mathbf{W}^O \quad (3.10)$$

$$\text{head}_i = \text{Attention}(QW_i^Q, KW_i^K, VW_i^V) \quad (3.11)$$

Where Q , K , V are respectively the Query, Key, Value vector. $\sqrt{D_k}$ is the scaled dot-product attention. \mathbf{W}^O , W_i^Q , W_i^K , W_i^V are respectively the corresponding linear mapping, which convert Q , K , V and the output to the specified dimension.

The MSA has a positive effect on helping the model identify the target objects and background, thus the neural network can learn more information from the target. LN is deemed to stabilize the deep network training, which can prevent unstable gradient, model degradation, etc. The module receives the 2d flattened patches from the image's patches. Due to it is different from CNN or RNN, apart from map the vectorized patches to D-dimensional embedding space, transformer needs to apply additional position encoding for retaining the patch's positional information.

3.2.2. Structure of TransUNet

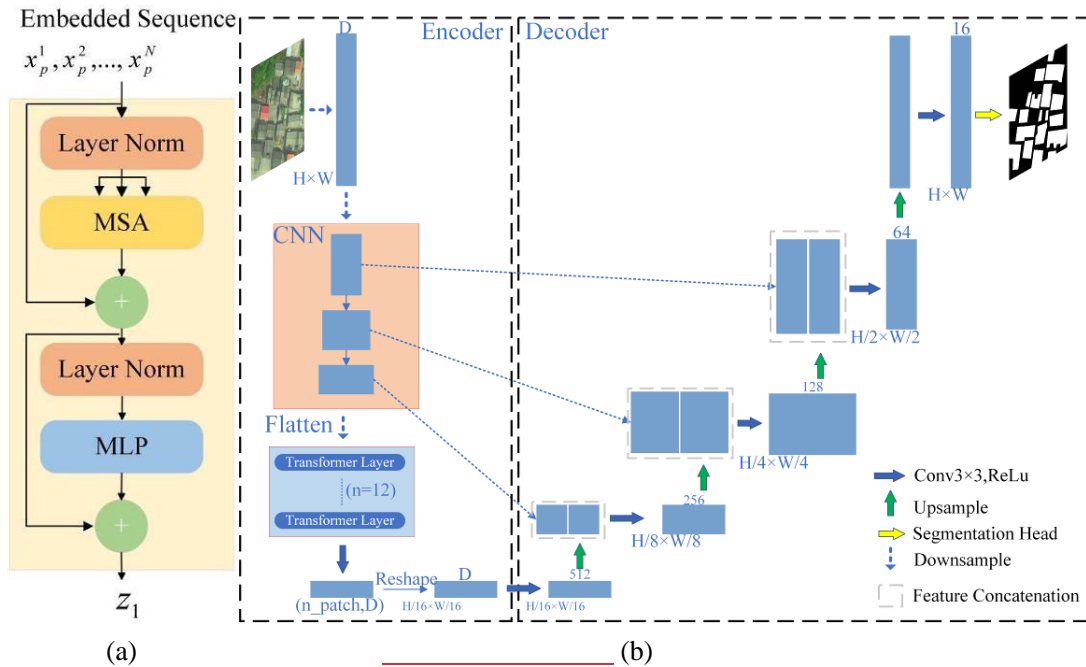
The overall structure of TransUNet is reference to U-Net, which is a U-shaped Encoder-Decoder structure, and the structure diagram is shown in the Fig. 3(b).

Encoder: the origin image is put into the CNN part for feature extraction, after the processing of position encoding and flatten, the patches are further put into the transformer module. The

374 transformer module consists of 12 transformer layers. The CNN part is implemented through
 375 using resnet50, which include 3 blocks in total, and each block output the hidden feature for skip
 376 connection.

377 Decoder: reshape the output sequence from encoder and then cascade up-sampling after
 378 transforming the number of channels. During the process, the skip connection is introduced by
 379 using the feature map hereinbefore. In the end, the segmentation result is generated.

380 In conclusion, TransUNet is the combination of U-Net and transformer, which is designed to
 381 make use of the advantage from both structures. The Global Attention from transformer can
 382 contribute to learn the global information, while the skip connection from U-shape network can
 383 contribute to get more information from shallow feature map output from CNN, and also CNN
 384 performs better in extracting the local information. In this research, buildings images are similar to
 385 medical images, with the features like high complexity level, large range of gray values. The skip
 386 connection structure can simultaneously acquisition of low-level semantic features and high-level
 387 semantic features, and transformer can conduce identify the buildings from background, thus
 388 TransUNet achieves a high accuracy in buildings segmentation.



389

390

391 **Fig. 3.** The overview of TransUNet framework (adapted from (Chen et al., 2021)): (a) Schematic
 392 diagram of Transformer layer; (b) Structure diagram of TransUNet

393

394 3.3. Building's height acquisition

395 UAV tilt photography modeling technology can combine control points encryption from
 396 massive image data with a small number of ground control points to obtain accurate external
 397 orientation elements (Kang et al., 2020). The conducted 3D model reflects the truly condition of
 398 the ground, and the data is selected to be in the WGS 1984 coordinate system. The ground
 399 resolution is one of the most intuitive and important parameters in tilt photography, and it's also a
 400 key factor determining the quality of the 3D modeling. In the process of performing aerial
 401 triangulation for tilt-image automation, it is necessary to ensure that the resolution of the different
 402 images is as consistent as possible while taking into account the resolution of the side-view image,
 403 thus to ensure accuracy and image overlap. Hence, the combinatory analysis of image resolution at

404 tilted viewing angle is required. The tilted image center point, near point and far point resolutions
 405 are expressed as follows:

$$\text{GSD}_{\text{top}} = \frac{\delta h \cos \beta_y}{f \cos(\alpha_y - \beta_y)} \quad (3.12)$$

$$\text{GSD}_{\text{mid}} = \frac{\delta h}{f \cos \alpha_y} \quad (3.13)$$

$$\text{GSD}_{\text{bottom}} = \frac{\delta h \cos \beta_y}{f \cos(\alpha_y + \beta_y)} \quad (3.14)$$

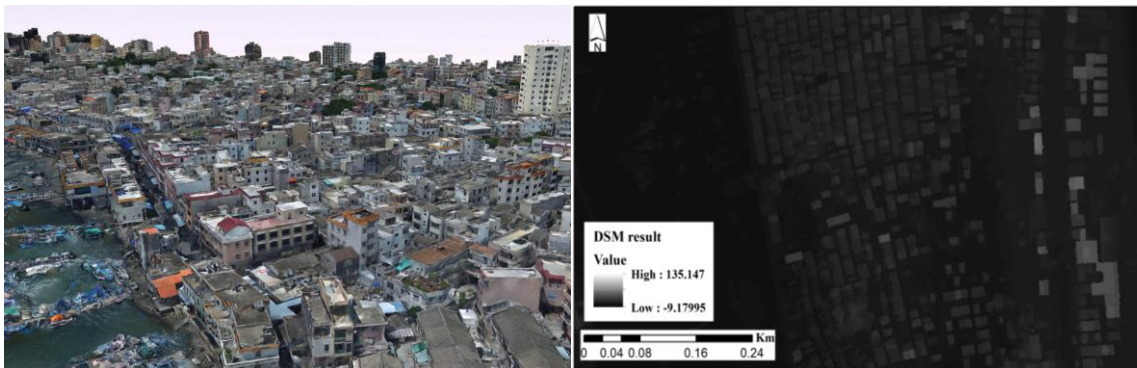
406 Where δ is sensor cell size, h is flight height, f refers to the camera focal length, α_y and
 407 β_y are respectively dip angle and half the angle of view. Normally, the ground resolution at the
 408 center of the tilted and vertical images should be comparable, and the minimum resolution of tilted
 409 images should less than three times the resolution of a vertical image.

410 There are multiple formats available for storing 3D models, including OBJ, STL, FBX,
 411 OSGB, etc. In this study, the generated 3D model is saved as OSGB format. OSGB format is
 412 originally proposed by Ordnance Survey for storing the geographic spatial data in the British. It
 413 combines binary encoding and compression algorithms to improve the data storage and
 414 transmission efficiency. Normally, the OSGB data contains information of geographic coordinates,
 415 elevations, texture mapping, and geometric shapes, which can be used to GIS application, virtual
 416 reality (VR), among others.

417 Digital surface model (DSM) is a digital terrain model that contains ~~more~~ elevation
 418 information about trees, buildings, and bridges. Compare to DEM, DSM can reflect the truly
 419 surface condition of earth, thus DSM has a wide range of application in city management or forest
 420 stewardship. In this research, the UAV data can be transformed to DSM data by using SuperMap
 421 software, and the DSM result is shown in Fig. 4(b). After generating the DSM, the elevations of
 422 the roof of the buildings and the corresponding elevations of the ground around the buildings are
 423 extracted by manual selection, then the height of buildings can be calculated by using equation
 424 (3.15).

$$\text{DSM}_{\text{Roof}} - \text{DSM}_{\text{Ground}} = H \quad (3.15)$$

425 Where DSM_{Roof} is the DSM value of the building's roof, $\text{DSM}_{\text{Ground}}$ represents the
 426 corresponding DSM value of ground, and H is the result of building's height.



427 (a) (b)
 428 **Fig. 4.** Building's height acquisition: (a) The schematic diagram of UAV tilt photography data; (b)
 429 The generated DSM results for Building height data extraction.
 430

431 3.4. Exposure and vulnerability assessment

432 The process of storm surge risk assessment involves two key components: exposure and
433 vulnerability. The exposure represents the elements exposed to hazardous spaces, while the
434 vulnerability refers to the level of the exposure elements' susceptibility to damage. When doing
435 exposure assessment, the disaster-affected elements can be conducted by overlaying the building
436 footprint data and land cover data with the hazard layer, which is the inundation data in this
437 research. The process can be accomplished using overlay analysis in ArcGIS software.

438 3.4.1. Adaptation of flood vulnerability functions.

439 Constructing an empirical stage-damage curve is a commonly used method for conducting
440 vulnerability assessments. However, as is mentioned above, China lacks of the data about flood
441 loss or insurance compensation in flood disasters, as a result, it's not practicable to develop
442 exclusive functions for the study region, so the depth-damage functions developed by Huizinga,
443 Joint Research Center (JRC) (Huizinga et al., 2017) are introduced. The depth-damage functions
444 manifest the loss ratio of the exposure elements in different inundation depth from 0 to 6 m, and
445 the ratio range from 0 to 1, which represents no damage to fully damaged. Besides, JRC also
446 provides the maximum economic losses per square meter for six different exposure element types
447 including residential, industrial, infrastructure, road, agricultural land, and transport. In this study,
448 the original functions and maximum loss data for China region are used, and the economic loss
449 can be calculated by multiplying the loss ratio, the maximum loss, and the disaster-affected area.

450 ~~The building's height is an important factor in flood loss estimation, normally the damage~~
451 ~~ratio decreases as the number of floors increases (Taramelli et al., 2022).~~ However, the JRC's
452 vulnerability functions do not provide the specific function of each height category. In this case,
453 the depth-damage functions in HAZUS are introduced. HAZUS is first released for earthquakes in
454 1997 by Federal Emergency Management Agency (FEMA), and that's when the HAZUS Flood
455 Model started to be developed (Scawthorn et al., 2006). In 2004, a multi-hazard version called
456 HAZUS-MH was a standardized GIS-based model that included the earthquake, flood, and
457 hurricane models (Nastev and Todorov, 2013). The HAZUS-MH flood model is designed
458 primarily for local and regional hazard planners and emergency managers for developing
459 emergency management plans and mitigation strategies (Tate et al., 2015). However, the depth-
460 damage functions in HAZUS-MH are restricted to regions within America, hence the HAZUS's
461 functions are introduced to adapt JRC's functions.

462 The approach to modifying functions is referred to the method proposed by Dabbeek et al.
463 (2020). In the process, the HAZUS loss ratios of each height category (one-story, two-story, three
464 and more-story) are averaged, which is shown in equation (3.16). Then the contribution of each
465 height category relative to the average loss is calculated as equation (3.17) shows. In the end,
466 multiplying the value obtained in the previous step by JRC's vulnerability functions yields the
467 adapted functions for each height category.

$$\bar{D}_{i(hazus)} = \frac{d_{i,1} + d_{i,2} + d_{i,3+}}{n} \quad (3.16)$$

$$i(depth) = \{(0, 6)\}$$

$$c_{i,h} = \frac{d_{i,h}}{\bar{D}_{i(hazus)}} \quad (3.17)$$

$$d_{i,h(adapted)} = c_{i,h} \times \bar{D}_{i(jrc)} \quad (3.18)$$

468 Where $d_{i,h}$ represents to the loss ratio at the inundation depth i for each height category h .
469 \bar{D}_i is the average loss ratio of all heights.

470

471 3.4.2. Quantitative risk assessment

472 The quantitative financial loss estimation is accomplished by overlaying the following data:
473 the inundation simulation result generated by FVCOM and SWAN modeling, the spatial
474 distribution of three types of exposure elements, the depth-damage functions of industrial and
475 commercial elements, and the adapted depth-damage functions for residential elements in three
476 height categories. The process of loss estimation can be shown in the following equation:

$$C = \sum_{i=1}^{i=n} D_{x(i)} f(d_i) A_i \quad (3.19)$$

477 Where C stands for the economic loss estimation result. n represents the total number of
478 exposure elements. $x(i)$ is the type of the i -th element and $D_{x(i)}$ is the maximum loss of the i -th
479 element. d_i is the depth of submergence of the i -th element and $f(d_i)$ is the loss ratio of the i -th
480 element. A_i refers to the area of the i -th element.

481 Comparing to the 984 euros per m^2 monetary loss of residential buildings in 2010, the
482 monetary loss of infrastructure and agriculture are respectively 12 euros per m^2 and 0.02 euro per
483 m^2 according to JRC, only account for 1% or less. Therefore, the monetary loss estimate of
484 infrastructure and agriculture is excluded in the study.

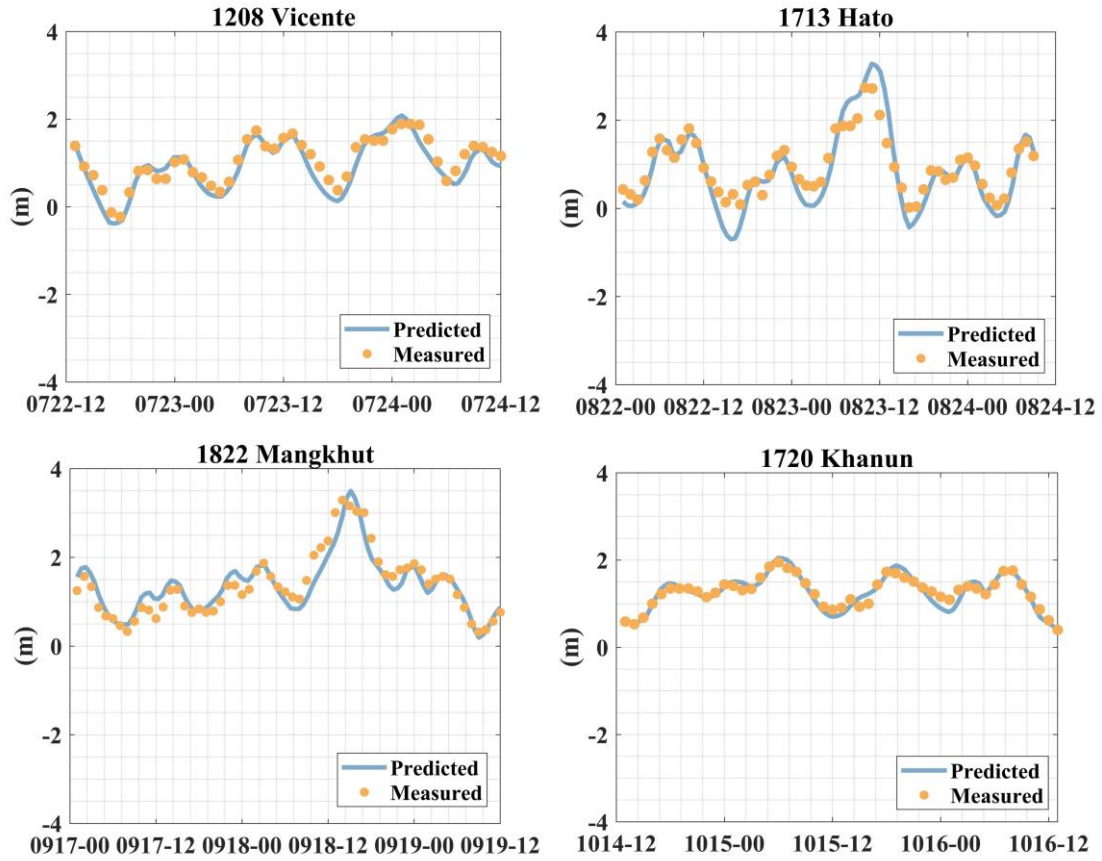
485 In this research, five storm surge scenarios are settled, ten administrative sub-zones are given
486 four different risk levels for each defined typhoon scenario.

487

488 4. Results and discussions

489 4.1. Validation

490 The performance of coupled FVCOM-SWAN model is evaluated. Four typical typhoons
491 (Vicente, Hato, Mangkhut, Khanun) are selected to validate the coupled model for the study region.
492 The measured data of each typhoon are captured by Department of Natural Resources of Huizhou
493 Bureau. Fig. 5 shows the maximum predicted water level and highest measured water level of the
494 chosen typhoons. Relative error and absolute error are introduced to evaluate the model and Table
495 1 displays the statistical results from Huizhou tidal station. It is seen that the predicted results are
496 in good agreement with the measurements. The statistic result shows that the relative errors of the
497 four typhoons range from 2.1% to 19.8%, and the absolute error varies from 4 cm to 54 cm.
498 Therefore, the coupled FVCOM-SWAN model demonstrates a reliable competence in
499 accomplishing the storm surge simulation task.



500
501 **Fig. 5.** The predicted water level and highest measured water level recorded by Huizhou tidal
502 station during different typhoon event
503

504 **Table 1.** The Relative error and Absolute error between maximum predicted water levels and highest
505 measured water levels from Huizhou tidal station during different typhoon events

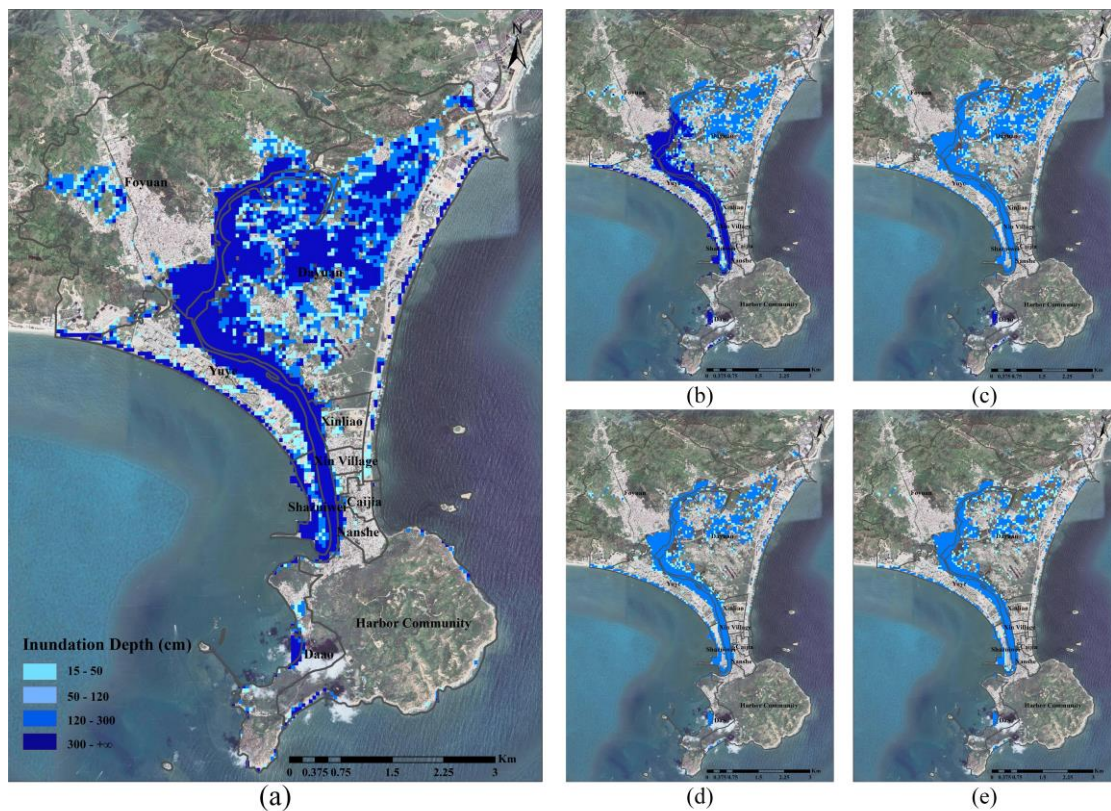
| Typhoon name | Measured data (cm) | Relative error (%) | Absolute error (cm) |
|-----------------|--------------------|--------------------|---------------------|
| Vicente (1208) | 189 | 10.3 | 19 |
| Hato (1713) | 274 | 19.8 | 54 |
| Mangkhut (1822) | 329 | 6.5 | 22 |
| Khanun (1720) | 201 | 2.1 | 4 |

506
507 *4.1. Hazard assessment*

508 In the present research, five storm surge inundation scenarios are defined, which represent
509 five different typhoon return periods: 10-year, 20-year, 50-year, 100-year, 1000-year respectively
510 corresponding to minimum central pressure 940hPa, 930hPa, 920hPa, 910hPa, 880hPa, and the
511 probability of occurrence are 10%, 5%, 2%, 1%, 0.1%. The simulation result is displayed through
512 ArcGIS 10.8 software, and the inundation area and depth simulation results for each scenario is
513 shown in Fig. 6. It is seen that the inundation area is spread over the coastal area in southwest of
514 study area. In particular, for the 1000-year return period scenario, the inundation area exceeds 13
515 km² in the study area. Moreover, the presence of Double-Moon Bay leads to the extension of the
516 inundation along the bay, contributing to severe disasters inland.

517 From the point of view of different scenarios, the area of inundation is in direct proportion to
 518 the typhoon's return period, and the proportion of inundation area increases from 14% to 31% of
 519 study area. When the return period is less than 50 years, most of the flooded area is considered to
 520 be in a high-level hazard zone, accounting for 75% for a 10-year return period and 67% for a 20-
 521 year return period, and no zone in very high-level hazard. Basically, the inundation area covers
 522 land such as grassland, saline land, and some buildings near the estuary as the area is more
 523 susceptible to flooding because of the lower elevation and drainage from the estuary. As the return
 524 period goes up to 100 years, 34% and 36% of the flooded area are defined at a high-level hazard
 525 and very high-level hazard. When it's 1000-year, the situation worsens with approximately half of
 526 the inundation area being considered in very high-level hazard. Typically, the flood extends from
 527 the margin of terrene, however, the southernmost region of the investigated area is characterized
 528 by a knoll covered by forest vegetation, which serves the dual purpose of water absorption and
 529 flood mitigation. In addition, the construction of embankments on both sides of Double-Moon Bay
 530 effectively withstands flooding. Nevertheless, because of the presence of the estuary, inadequate
 531 water absorption ability of coastal saline soil and the hydrological system, the inundation flows in
 532 through the estuary and spreads inland.

533



534

535 **Fig. 6.** The storm surge inundation simulation results of five different typhoon scenarios: return period
 536 (a) 1000-year, (b): 100-year, (c): 50-year, (d): 20-year, (e): 10-year. The base map is obtained from ©
 537 GoogleMaps (map data © 2023 Google)The storm surge inundation simulation results of different
 538 typhoon scenarios. The base map is obtained from © GoogleMaps (map data © 2023 Google).

539

540 4.2. Buildings' characters extraction

541 — Buildings are places where human populations gather and distribute, and contain amounts of

property, which have great significance in quantitative risk assessment.

4.2.1 TransUNet model training

The dataset construction area is chosen at southwest waterfront region of Renshan Town. The specific location is shown in Fig. 7. The chosen area is a typical area of the Huizhou coastal area. Apart from the seaside bungalows, the area contains some high-rise buildings that are identified as commercial hotels or resorts, while dense residential area is also widely distributed throughout the inland region. In conclusion, the chosen area contains different kinds of buildings with strong representativeness. Since most of the buildings in China coastal towns have the similar characters, the model trained on the representative region has the ability to identify buildings in other regions rapidly.

The labels of the buildings in the area are generated by manually annotation, and the image is cropped into small patches with a size of 256*256. The labels of the buildings in the area are generated by manually annotation, and the image is cropped to pixels with a size of 256*256. Besides, some of the images without buildings are filtered for preventing the effect of imbalance between the building samples and background samples. In the end, a total of 1200 labeled building dataset is constructed, and the dataset size is deemed sufficient when compared to previous study (Dixit et al., 2021; Ji et al., 2018). The dataset is then divided into a training set and a test set, with the ratio of 8:2. Data enhancement techniques, such as random hue saturation value, random shift scale ~~rotation~~rotate, flip, and ~~rotation~~rotate, are implemented during model training to improve the deep learning model's generalization performance and prevent overfitting.

The training's initial learning rate is set to 1e-5, and the learning rate adjustment strategy for improved training. The batch size is specified as 4, and the number of training epoch is 100. The model is trained on a NVIDIA RTX3060 GPUs.

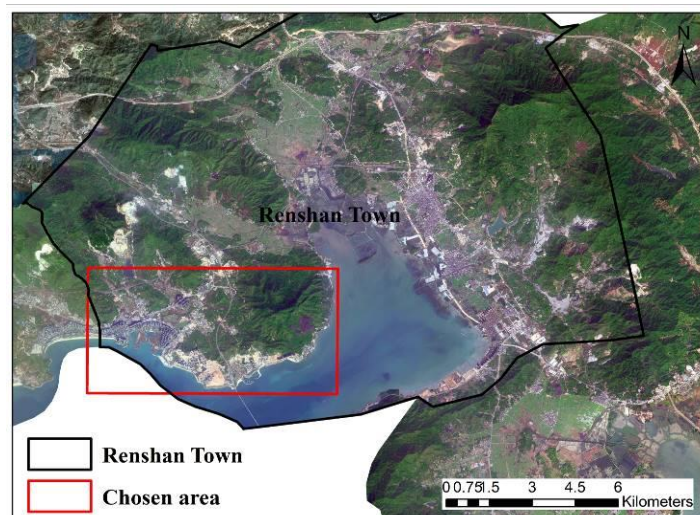


Fig. 7. The chosen area to make the training samples. The base map is obtained from © GoogleMaps (map data © 2023 Google).

4.2.2. Extraction result

Several effective indicators are introduced, including Recall, Precision, F1-score, and mean Intersection-over-Union (mIoU), to evaluate the performance of the deep learning model. Recall is the probability of being predicted as positive among actual positive samples. Precision, on the other hand, is the probability of being actually positive among samples predicted as positive. F1-score serves as an indicator that achieves a balance point between precision and recall, essentially

575 being the harmonic average of precision and recall. mIoU is the mean ratio of the intersection to
 576 the union between predicted and true values for each category. True positive (TP) indicates the
 577 true samples that are predicted correctly by the model. False positive (FP) indicates the positive
 578 samples that the model incorrectly predicted. True negative (TN) and false negative (FN) refer to
 579 the number of samples that are correctly and incorrectly predicted as negative by the model. The
 580 equations of Recall, Precision, F1-score, and mIoU are as follows:

$$recall = \frac{TP}{TP + FN} \quad (4.1)$$

$$precision = \frac{TP}{TP + FP} \quad (4.2)$$

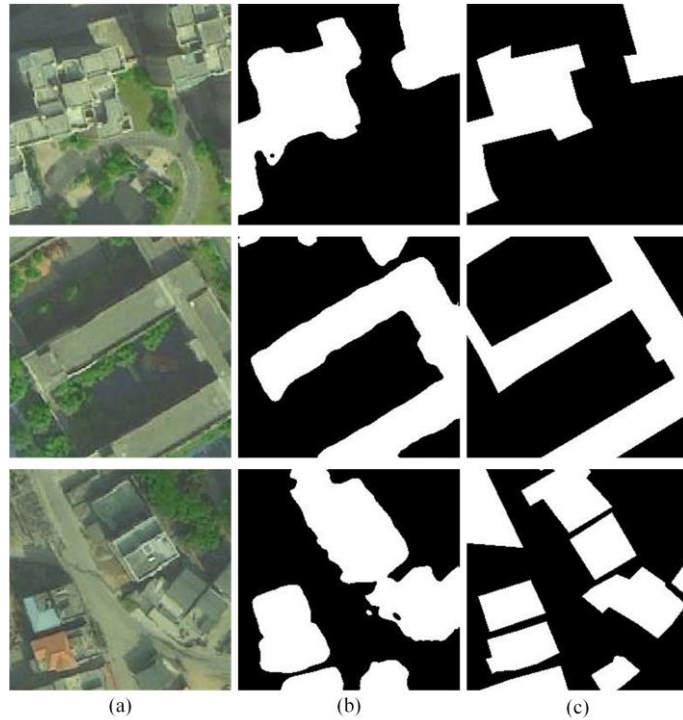
$$F1 = 2 \times \frac{precision \times recall}{precision + recall} \quad (4.3)$$

$$mIoU = \frac{1}{k+1} \sum_{i=0}^k \frac{TP}{TP + FP + FN} \quad (4.4)$$

581 The quantitative evaluation result is shown in Table 2, and the visualization results are
 582 illustrated in Fig. 8. As Table 2 shows, the recall score reaches 87% indicating that most of the true
 583 building pixels are predicted correctly, and Precision indicates that 82% of all building pixels are
 584 correctly detected. Moreover, both the mIoU score and F1-score exceed 80% manifest that the
 585 model can balance well between precision and recall. These results reflect the strong performance
 586 of TransUNet in the building extraction task. After post-processing the result, such as boundary
 587 simplification, the building vectorization results can be used for further research in risk assessment.
 588 The overall result is shown in Fig. 9 [\(b,c\)](#).

589 **Table 2.** The statistical accuracy assessment of building footprint extraction

| Evaluation metric | |
|-------------------|-------|
| Recall (%) | 87.03 |
| Precision (%) | 82.04 |
| F1-score (%) | 84.46 |
| mIoU (%) | 83.38 |



590

591 **Fig. 8.** Building footprint extraction result in study area. (a) Remote sensing images obtained from
 592 Jilin-1 satellite (© Chang Guang Satellite technology CO., LTD); (b) Extraction result; (c) Ground
 593 truth. The building is marked in white, and the background is marked in black
 594

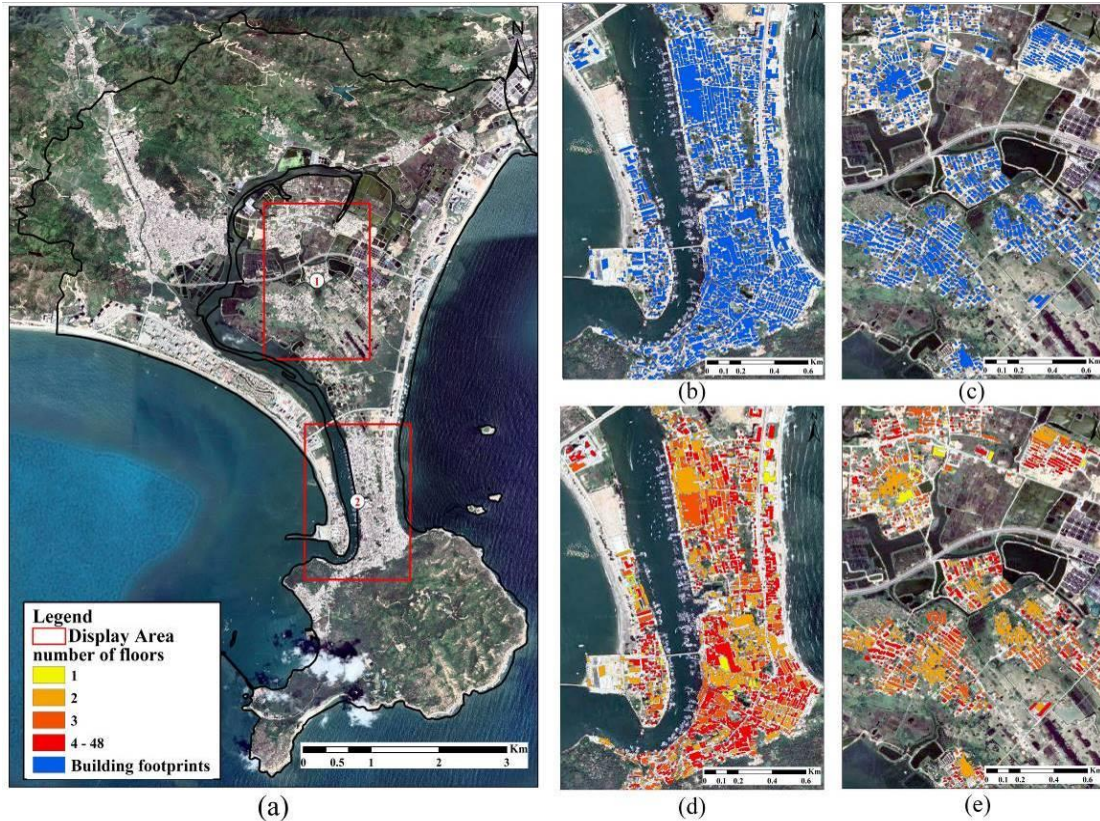
595 *4.2.3. Building height calculation*

596 Through combing two methods mentioned above, the height information is acquired in units
 597 of meters. The number of floors is derived by dividing the acquired height information by the
 598 specified standard height of 3 meters, according to the China residential design standards. The
 599 general condition of building floor is shown in Table 3. Just as mentioned above, the buildings in
 600 study area are mainly for residential and commercial use. Since the study area is undeveloped, the
 601 high buildings and large mansions is relatively less common, and most of them are built for
 602 seaside resort. Instead, buildings with 5 floors or less are the mainstream in study area as respected,
 603 which the proportion can reach 76.5%. The building footprint extraction result and building's
 604 height information extraction result can be found in Fig. 9 (d,e).

605

Table 3. Statistical results of building height in the study area

| Building floor | Area (m ²) | Proportion (%) |
|----------------|------------------------|----------------|
| 1-5 | 17537238.61 | 76.5 |
| 6-10 | 4996897.08 | 21.8 |
| 11-20 | 342207.82 | 1.5 |
| 20+ | 54083.93 | 0.2 |



606

607 **Fig. 9.** The building characters extraction result: (a) The schematic of the display area; (b, c)
 608 Building footprint result in area 1 and 2; (d, e) Building height result in area 1 and 2. The base
 609 map is obtained from © GoogleMaps (map data © 2023 Google).

610

611 *4.3. qualitative risk assessment*

612 Risk matrix is a risk assessment approach firstly developed by Electronic System Center,
 613 which was originally to assess the risk in the life cycle of purchase project (Garvey and
 614 Lansdowne, 1998). An additional qualitative risk assessment is conducted using the risk matrix
 615 method, incorporating improved land use data to highlight the superiority of building extraction in
 616 flood risk assessment. [The concrete representation of the risk matrix is shown in table 4.](#)

617

Table 4. The concrete representation of the risk matrix

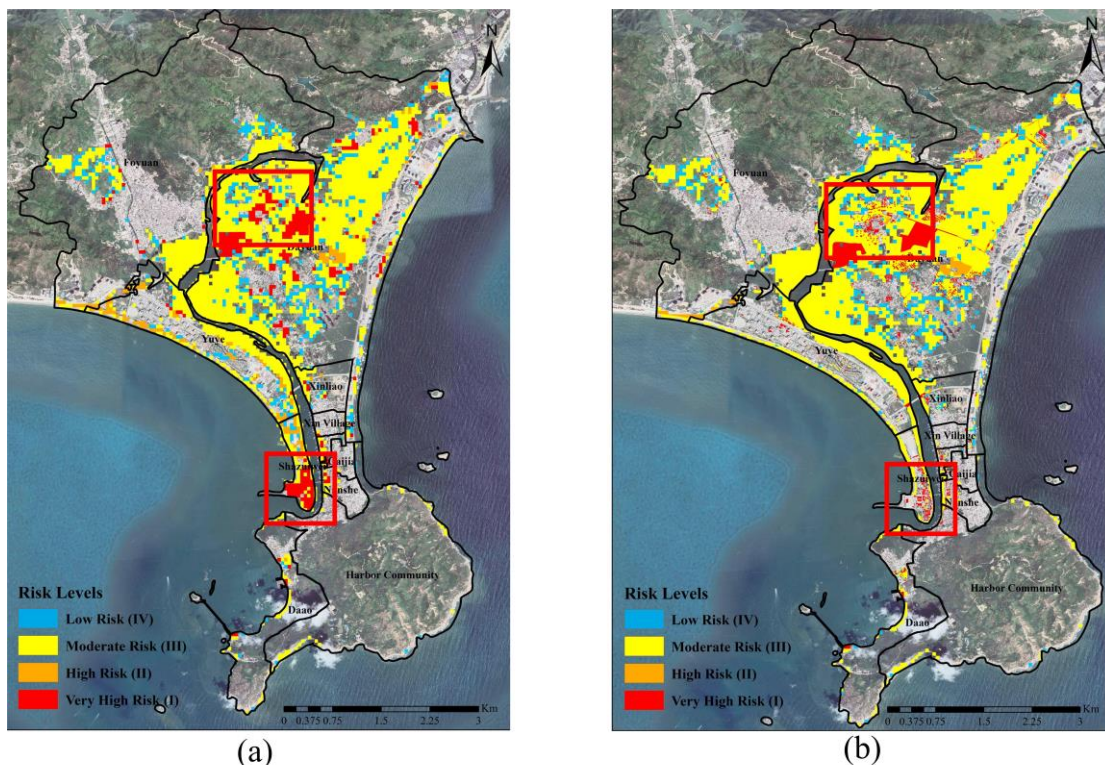
| | | <u>Vulnerability</u> | | | |
|---------------|------------------|----------------------|-----------------|------------------|------------------|
| | | <u>Low</u> | <u>Moderate</u> | <u>High</u> | <u>Very High</u> |
| <u>Hazard</u> | <u>Low</u> | <u>Low</u> | <u>Low</u> | <u>Moderate</u> | <u>Moderate</u> |
| | <u>Moderate</u> | <u>Low</u> | <u>Moderate</u> | <u>High</u> | <u>High</u> |
| | <u>High</u> | <u>Moderate</u> | <u>High</u> | <u>High</u> | <u>Very High</u> |
| | <u>Very High</u> | <u>Moderate</u> | <u>High</u> | <u>Very High</u> | <u>Very High</u> |

618

619 As is shown in Fig. 10(a), the concentrations of organic town of Dayuan village and
 620 Shazuiwei makes it in very high vulnerability level. Under the circumstance of defined 880hPa
 621 storm surge scenario, the inundation area spread inland which makes the majority area of Dayuan
 622 is regarded as moderate risk, and a fraction of the only very high risk area is distributed in
 623 Shazuiwei and north of Dayuan village. In the area of Yuye village, part of the south coastal area is

624 considered in moderate or high risk level. That is mainly because the majority area of Yuye is
 625 defined as resort district except for a few areas of tidal flats, which is in high vulnerability.
 626 However, after referring to the result of hazard assessment, buildings in the area are not actually
 627 inundated, meaning the area should not be at risk level.

628 Through comparing the Fig. 10(a) and Fig. 10(b), the enhanced land use data in the present
 629 research demonstrates a higher ability to recognize vulnerability elements, which the type is
 630 buildings in the present research. The two red boxes in the figure highlight the noticeable disparity
 631 between the original and current results. The present risk assessment provides more refined risk
 632 assessment result compared to the original result, as the previously identified large hazardous
 633 areas are replaced with more detailed and smaller zones. This refinement is conducive for
 634 government or decision-makers to conduct disaster prevention measures, propose quick guidance
 635 for personnel evacuation and organize rescue operations in the event of a disaster.



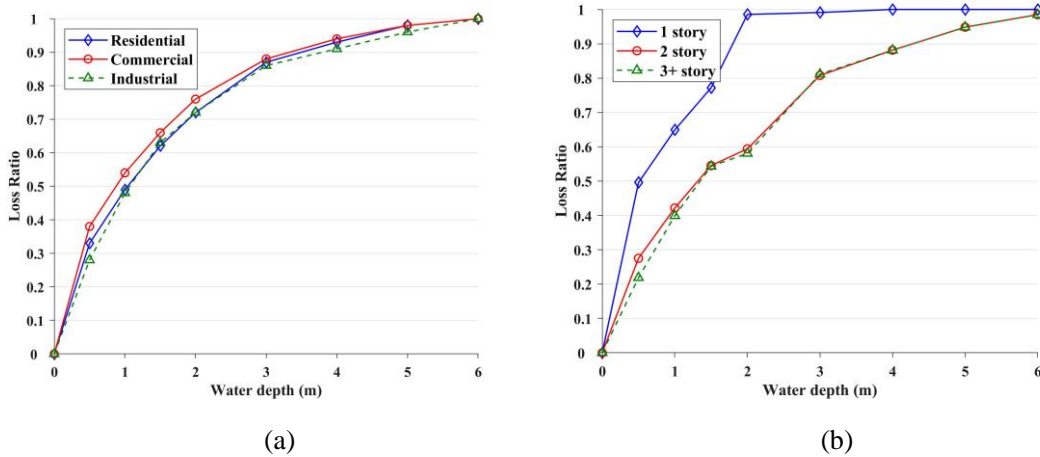
636
 637 **Fig. 10.** The risk assessment maps before (a) and after (b) improvement for storm surge scenarios
 638 of 1000-year return period. The base map is obtained from © GoogleMaps (map data © 2023
 639 Google).

640 4.4. JRC's depth-damage function adaption

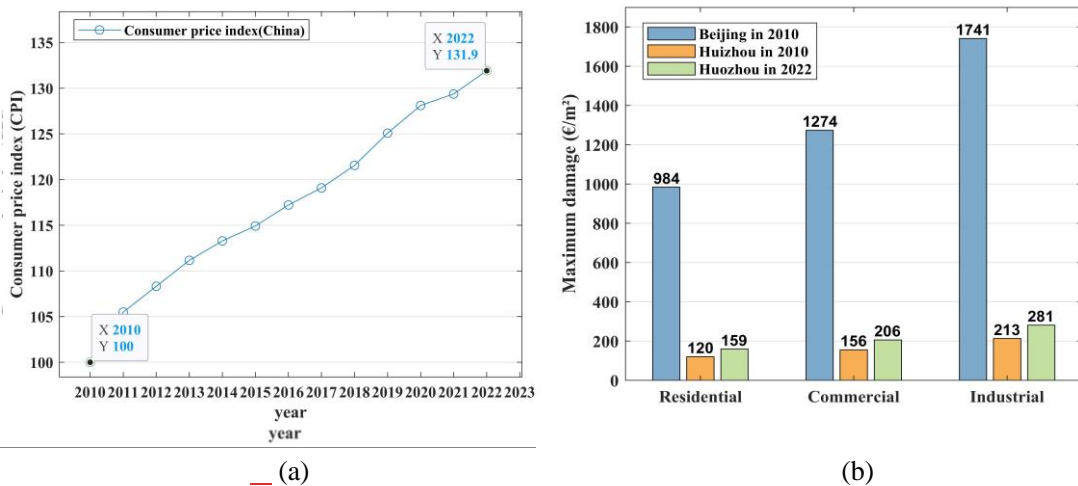
642 Fig. 11 illustrates the damage ratio given flood-depth after adjustment, respectively for one-,
 643 two- and more than three-story residential buildings. After adjustment, the damage of one-story
 644 residential building function is significantly enhanced, and the loss ratio reach 1 early, which is
 645 explicable as 2m-depth flood almost submerges the entire building, resulting in a potential loss of
 646 the maximum property value. On the contrary, the loss ratio for multi-story residential building is
 647 decreased relative to the original function, it reaches the same level as in the original function
 648 when the water depth reaches 5 meters. Furthermore, the function of a two-story residential
 649 building is quite similar to that of a building with three or more stories. This can be attributed to

650 the flood's effect on buildings with six meters or less depth being nearly the same, on account of
 651 the flood can't overwhelm the entire buildings.

652 The Joint Research Centre provides information on the maximum damages per square for
 653 each type of building. This refers to the maximum monetary damage incurred when buildings are
 654 inundated, which is the monetary damage value when the damage ratio in the depth-damage curve
 655 reaches 100%. Although ~~JRC provides~~ the maximum monetary damages are provided, they are
 656 computed for Beijing in 2010. However, there is a substantial difference in the level of
 657 development between Beijing and the study area. For better matching the financial level in study
 658 area, adjustment can be achieved based on scaling the maximum monetary damage value with the
 659 GDP ratio according to Huizinga (2007). Based on the 2010 GDP of Beijing of 14113558 million
 660 yuan and the GDP of Huizhou of 172995 million yuan, the maximum monetary damage is
 661 adjusted by equal proportions. Besides, the price level also needs to be adjusted to the 2022 price
 662 level. According to the World Bank, the Chinese consumer price index (CPI) has changed from
 663 100 in 2010 to 131.9 in 2022, the tendency of variation and the adjusted maximum monetary
 664 damages are shown in Fig. 12.



665
 666 (a) (b)
 667 **Fig. 11.** (a) The depth-damage functions proposed by JRC; (b) The adapted depth-damage
 668 functions for residential buildings in different floors
 669



670 (a) (b)
 671 **Fig. 12.** (a) The variation trend of Consumer price index released by World Bank; (b) The
 672 maximum monetary damage per m² for each type of exposed elements in China (in 2010 and in

673

674

675 *4.5. Quantitative risk assessment*

676 Loss assessments of five storm surge scenarios are computed for return periods of 10, 20, 50,
677 100, and 1000 years, through employing the method in section 3. The estimate monetary damage
678 is summarized in Table 45.

679 The statistical data in Table 4-5 demonstrate an increase in the affected area and total
680 economic loss with an increasing return period. Comparing to the total affected area of 131533.12
681 m² and the total economic losses of 9330517.49 euros with the 10-year return period, the
682 corresponding estimate result with 1000-year return period is 917437.99 m² and 68364923.25
683 euros, which is both approximately seven times higher. This indicates a proportional
684 relationship between the extent of regional impairment and the return period of a typhoon.
685 Although the impacted area for the 20-year and 50-year return periods exhibits relative
686 proximity as the different is 24118.26 m², there is still a significant disparity in economic
687 losses. According to the inundation result above, that's because the inundation area of two
688 return period is nearly the same except for the slight difference in the northeast of the study
689 region, but the flood depth of 50-year intensified, which causes more monetary damage. In
690 terms of inundated building types, in case that study area is characterized as a tourism and
691 fish breeding area, the proportion of economic losses in industrial is relatively low. The losses
692 of residential buildings and commercial buildings is comparatively close, up until the severity
693 of storm surge reach 50-year return period. At this point, the losses experienced by residential
694 buildings exceed those incurred by commercial buildings by more than double. The fact can
695 be explained by the commercial buildings area mainly constructed by the seaside for better
696 turnover therefore both types of waterfront buildings is impacted. However, as the severity of
697 the typhoon worsens, more residential settlements inland are flooded, resulting in a swift
698 increase in economic losses for residential buildings.

699 **Table 45.** The statistic result of the quantitative risk assessment for five defined typhoon scenarios.

| Scenario | Elements | Area (m ²) | Economic losses (€) | Total losses (€) | Probability | Risk (€) |
|--------------------|-------------|------------------------|---------------------|------------------|-------------|-----------|
| 10-year (940hPa) | Residential | 94847.11 | 4910882.27 | 9330517.49 | 0.1 | 933051.75 |
| | Commercial | 36163.62 | 4281840.09 | | | |
| | Industrial | 522.39 | 137795.12 | | | |
| 20-year (930hPa) | Residential | 216010.31 | 7872861.19 | 13665211.91 | 0.05 | 683260.60 |
| | Commercial | 55423.59 | 5602828.01 | | | |
| | Industrial | 522.39 | 189522.71 | | | |
| 50-year (920hPa) | Residential | 237572.35 | 16509796.15 | 24607011.73 | 0.02 | 492140.23 |
| | Commercial | 57979.81 | 7775321.70 | | | |
| | Industrial | 522.39 | 321893.88 | | | |
| 100-year (910hPa) | Residential | 291759.48 | 19857901.69 | 28446797.47 | 0.01 | 284467.97 |
| | Commercial | 75123.51 | 8194736.70 | | | |
| | Industrial | 833.39 | 394159.08 | | | |
| 1000-year (880hPa) | Residential | 762570.09 | 49295364.67 | 68364923.25 | 0.001 | 68364.92 |
| | Commercial | 149457.01 | 17907591.59 | | | |
| | Industrial | 5410.89 | 1161967.00 | | | |

700

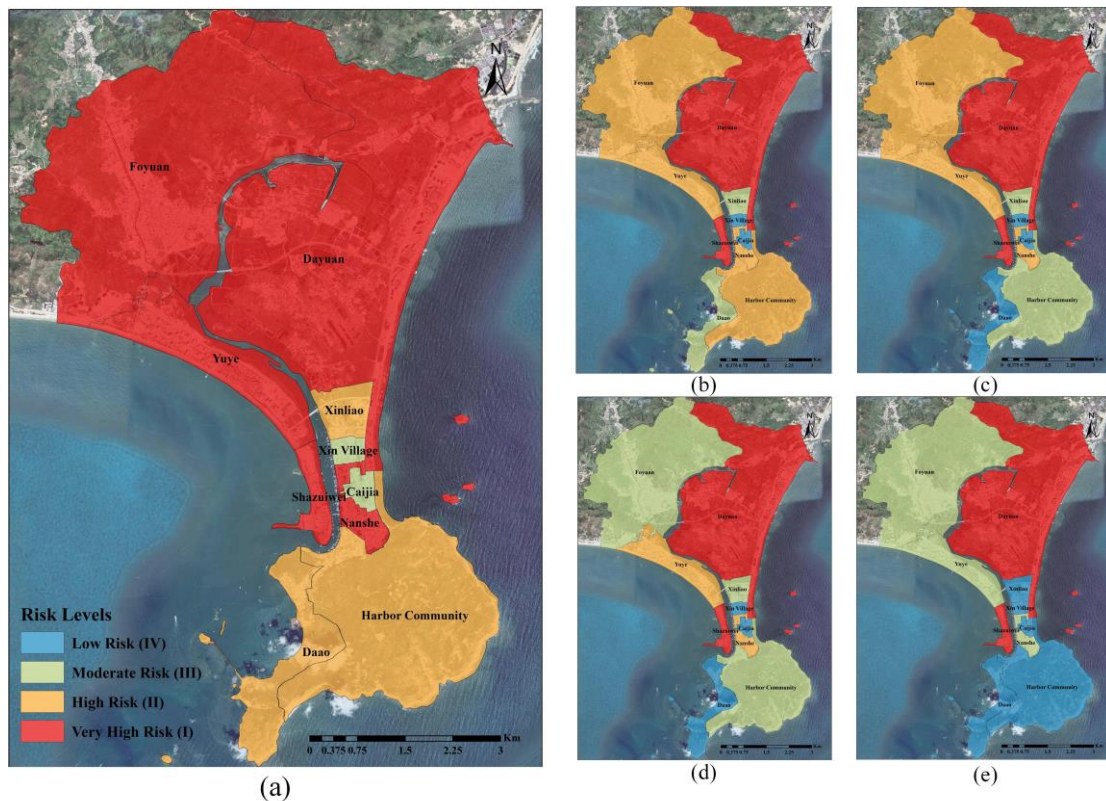
701 Based on the economic losses estimation result for five storm surge scenarios, through using
702 zonal statistics method on the data of administrative sub-zones in the study area, the quantitative
703 risk assessment is conducted. The economic losses and spatial distribution of storm surge risk for
704 ten sub-zones in five different scenarios are shown in Fig. 13. The zonation statistics result map of
705 each sub-zone is defined at four different risk levels (very high, high, moderate, low). The
706 classification of risk levels is obtained by categorizing all zonal statistic result based on quantiles.

707 As is shown in Fig. 13, Dayuan village is considered in very high risk for every defined
708 typhoon scenario. Through analyzing the geographical characteristics of the study area, it can be
709 found that although Dayuan is a relatively inland village, it's surrounded by the watercourse of the
710 estuary of Double-Moon Bay. Due to the existence of flood control dam, both side of the bay offer
711 a measure of protective effectiveness, which result in the water level rises in inland watercourse,
712 and further causes flooding of residential buildings in Dayuan village, leading to massive financial
713 losses. In contrast, Foyuan village is also a village with a relatively large area, the risk is at
714 moderate level for 10, 20-year return period, and the level escalates to high for 50, 100-year return
715 period and reaches very high in 1000-year. Considering the presence of the knoll, the spread of
716 inundation is hindered. However, as typhoon becomes more severe, the inundation hit the western
717 buildings in the region, which led to the phenomenon of progressively escalating risk level. In
718 terms of those villages with relatively smaller sizes, due to the protection of dam, Xinliao village,
719 Xin village, Caijia village all are defined in relatively low risk level, although the regions with a
720 high density of buildings. Shazuiwei and Yuye village in different return period are considered in
721 different risk level, the cause of this phenomenon might be that apart from the higher density of
722 buildings, the buildings in Shazuiwei are distributed in coastal area, combing the impact of
723 inundation of both sides as it's located at the outermost part of the gulf. Consequently, the risk
724 level in Shazuiwei remains consistently high as opposed to gradually increasing like in Yuye
725 village. Although they are located at the outermost part of the study area, the quantitative risk level
726 of Daa village and Harbor community is gradually increasing for different return period, but it's
727 not as serious as the other village, which can be explained that these locations exhibit elevated
728 topography.

729 Comparing the qualitative risk assessment result and the quantitative risk assessment result,
730 the first difference to be noticed is that the two results focus on different scales. For the qualitative
731 result, the emphasis is on delineating the regions in different risk levels, which leads to the
732 prevention and control of priority areas. Whereas for quantitative result, the scale of the result is
733 limited to the village level zoning, as the estimated monetary loss amounts are summarized at the
734 village level. Furthermore, while the qualitative results suggest that certain regions may not be at a
735 moderate or high risk level, the quantitative result reveals that the estimated monetary loss for
736 those villages are not insignificant. In conclude, the qualitative risk assessment provides new
737 results from a completely different perspective than qualitative risk assessment. The results can
738 provide intuitive information about the potential monetary loss to the secondary government
739 departments, thus to help provide constructive suggestions in terms of risk prevention and control.

740 The quantitative risk assessment and zonal risk maps can assist the government or decision-
741 makers in recognizing the specific economic losses of each sub-zones, so it's helpful to identify
742 the areas that are more susceptible to experiencing significant losses, which allows them to
743 develop disaster prevention measures, for example constructing disaster prevention facilities,
744 budget allocation for disaster prevention and planning evacuation strategies. Besides, establishing

745 the quantitative risk for different typhoon periods can enhance the decision makers understanding
 746 of the potential vulnerability in each sub-zone, and facilitates the implementation of appropriate
 747 preventive and disaster relief measures facing different typhoon intensity.



748
 749 **Fig. 13.** The zonation maps of the quantitative risk assessment for five defined typhoon scenarios:
 750 return period (a) 1000-year, (b): 100-year, (c): 50-year, (d): 20-year, (e): 10-year. The base map is
 751 obtained from © GoogleMaps (map data © 2023 Google).

752 **5. Conclusions**

753 These years, the academic research on storm surge risk assessment has been greatly
 754 developed due to climate change and financial growth in coastal area. However, the quantitative
 755 risk assessment is inexecutable in the undeveloped area since on account of the lacks of building
 756 characters and damage assessment data. Target at the question above, the purpose of this paper is
 757 to propose a method for conducting refined storm surge risk assessment quantitatively based on
 758 deep learning and GIS techniques. Firstly, the reliable coupled FVCOM-SWAN model is utilized
 759 to simulate five defined storm surge scenarios. Facing the challenge of the absence of data, a deep
 760 learning method TransUNet is applied to extract the building footprint data for refined extraction
 761 of exposed elements, and buildings' height data is acquired through UAV. To compensate for that
 762 the available depth-damage functions do not taking building's height into account, the functions
 763 are adjusted for buildings with different floor and consequently to perform more refined monetary
 764 losses calculations in five defined scenarios. Eventually, the quantitative risk assessment and
 765 zonation maps of the study area are generated base on GIS techniques

766 The quantitative risk assessment result of the study region shows that on account of the
 767 existence of estuary and the gathering of buildings, Dayuan village presents the high-risk level in
 768 all defined typhoon scenario, and the economic loss risk is large. The flood control dam provides
 769 protection of Xinliao village, Xin village, Caijia village, which prevents the regions suffering large

770 economic losses as the typhoon return period is 10-year and 20-year. However, the storm surges,
771 under the typhoon scenarios that the return period is greater than 50-year, can overwhelm the
772 existed dikes, and both the commercial buildings and residential buildings suffer heavy economic
773 losses. Therefore, it's necessary to make land use planning and adjustment especially in Dayuan
774 and Shazuiwei as they are under very high-risk level to prevent the impact and losses caused by
775 storm surges. Besides, the regions that is nearest to the sea doesn't mean they suffer greater
776 potential economic loss, as the risk level of Daa village and Harbor community are considered at
777 a relatively low level because of the topographical characteristics and the distribution of buildings.

778 In the context of global warming and increased climate extremes, the occurrence of large-
779 scale typhoons has become more frequent, such as Typhoon Rammasun and Typhoon Meranti
780 (corresponding to 100-year return period). Therefore, the modified typhoon parameters are utilized
781 for simulation five typhoon scenarios, in order to assuming the different storm surge disaster
782 situation in the future. On the basis of the above, ~~The~~ the study provides a framework for refined
783 quantitative storm surge risk assessment targeting the problem of acquiring exposure elements and
784 the establishing multi-variable empirical depth-damage functions, as a consequence of missing
785 data in underdeveloped regions. The generated results can help the decision-makers to identify the
786 areas that are susceptible to experiencing significant losses efficiently, and help the respective
787 authorities with disaster prevention, future land use planning and material deployment.
788 Furthermore, it is important to remark that, the methodology of this paper has general applicability,
789 since the applied models are publicly available. Thus, there is also potential for further application.
790 For example, the framework can be applied in other coastal areas in China, as they have similar
791 characters, which also means there is a possibility to utilize in larger scales. Furthermore, the
792 framework can also be performed in other types of disasters, such as flood, earthquake, and
793 mudslide. Consequently, the proposed methodology demonstrates an extensive relevance to the
794 scientific community.

795 There is still room for improvement in this study. The current study relied on manual labeling
796 in terms of distinguishing between functional areas to conduct risk assessment. In the future study,
797 efforts will be made to distinguish the types of exposure elements in a more objective way, based
798 on diverse data sources such as social media Point Of Interest (POI). Additionally, exploring the
799 activity patterns of the population through multiple sources of data including taxi trajectories and
800 smart cards can contribute to the consideration of population risks in different storm surge
801 scenarios, thereby prompting more comprehensive risk assessments.

802 803 **Data availability.**

804 Remote sensing images are obtained from Chang Guang Jilin-1 satellite. The dataset of wind field
805 is generated by ERA5 and Holland method. The Administrative Boundary data is obtained from
806 National geographic information public service platform. The datasets can be obtained from
807 <https://dx.doi.org/10.6084/m9.figshare.24586605> (Yu, 2023). DEM data and UAV data are
808 obtained from Department of Natural Resources of Huizhou Bureau, data sets are not publicly
809 available due to the policy of the Natural Resources of Huizhou Bureau.

810
811 Competing interests. The authors declare that they have no conflict of interest.

812 813 **Authorship contributions.**

814 **Lichen Yu:** Investigation, Methodology, Data Curation, Visualization, Formal analysis, Writing -
815 Original Draft. **Shining Huang:** Investigation, Data Source, Data Curation, Visualization, Formal
816 analysis. **Hao Qin:** Conceptualization, Methodology, Validation, Supervision, Writing - Original
817 Draft, Project administration, Funding acquisition. **Wei Wei:** Validation, Data Curation,
818 Visualization. **Lin Mu:** Conceptualization, Supervision, Project administration, Funding
819 acquisition.

820

821 Acknowledgement

822 [This work was supported by Shenzhen Science and Technology Program \(Grant No.](#)
823 [KCXFZ20211020164015024\), National Natural Science Foundation of China \(Grant No.](#)
824 [52101332\) and Guangdong Basic and Applied Basic Research Foundation \(Grant No.](#)
825 [2024A1515011805, 2023A1515240047, 2024A1515012032\)](#)~~This work was supported by~~
826 ~~[Shenzhen Science and Technology Program \(Grant No. KCXFZ20211020164015024\), National](#)~~
827 ~~[Natural Science Foundation of China \(Grant No. 52101332\) and Guangdong Basic and Applied](#)~~
828 ~~[Basic Research Foundation \(Grant No. 2023A1515240047\).](#)~~ This work was supported by the
829 ~~[Shenzhen Science and Technology Program \(Grant No. KCXFZ20211020164015024\), National](#)~~
830 ~~[Key Research and Development Program of China \(Grant No. 2021YFC3101800\), National](#)~~
831 ~~[Natural Science Foundation of China \(Grant No. 52101332 and U2006210\).](#)~~

832

833 References

834

835 Adnan, M. S. G., Abdullah, A. Y. M., Dewan, A., and Hall, J. W.: The effects of changing land use and
836 flood hazard on poverty in coastal Bangladesh, *Land Use Policy*, 99, 104868, 2020.

837 Armenakis, C. and Nirupama, N.: Estimating spatial disaster risk in urban environments, *Geomatics,*
838 *natural hazards and risk*, 4, 289-298, 2013.

839 Booij, N., Holthuijsen, L. H., and Ris, R. C.: The "SWAN" wave model for shallow water, in, 668-676,
840 1996.

841 Chen, C., Liu, H., and Beardsley, R. C.: An unstructured grid, finite-volume, three-dimensional,
842 primitive equations ocean model: application to coastal ocean and estuaries, *Journal of atmospheric and*
843 *oceanic technology*, 20, 159-186, 2003.

844 Chen, D. and Gao, G. X.: Probabilistic graphical fusion of LiDAR, GPS, and 3D building maps for
845 urban UAV navigation, *Navigation*, 66, 151-168, 2019.

846 Chen, J., Lu, Y., Yu, Q., Luo, X., Adeli, E., Wang, Y., Lu, L., Yuille, A. L., and Zhou, Y.: Transunet:
847 Transformers make strong encoders for medical image segmentation, *arXiv preprint arXiv:2102.04306*,
848 2021.

849 China Marine disaster bulletin: Historical Marine disasters in China, available at:
850 <http://www.mnr.gov.cn/sj/sjfw/hy/gbgb/zghyzhgb/>, last access: 12 November 2023.

851 Comber, A., Umezaki, M., Zhou, R., Ding, Y., Li, Y., Fu, H., Jiang, H., and Tewkesbury, A.: Using
852 shadows in high-resolution imagery to determine building height, *Remote Sensing Letters*, 3, 551-556,
853 10.1080/01431161.2011.635161, 2011.

854 Dabbeek, J., Silva, V., Galasso, C., and Smith, A.: Probabilistic earthquake and flood loss assessment in
855 the Middle East, *International Journal of Disaster Risk Reduction*, 49, 101662, 2020.

856 de Moel, H. and Aerts, J. C. J. H.: Effect of uncertainty in land use, damage models and inundation
857 depth on flood damage estimates, *Natural Hazards*, 58, 407-425, 2011.

858 Dixit, M., Chaurasia, K., and Kumar Mishra, V.: Dilated-ResUnet: A novel deep learning architecture
859 for building extraction from medium resolution multi-spectral satellite imagery, *Expert Systems with*
860 *Applications*, 184, 115530, 2021.

861 Fang, J., Wahl, T., Fang, J., Sun, X., Kong, F., and Liu, M.: Compound flood potential from storm surge
862 and heavy precipitation in coastal China: dependence, drivers, and impacts, *Hydrology and Earth*
863 *System Sciences*, 2021.

864 Frantz, D., Schug, F., Okujeni, A., Navacchi, C., Wagner, W., van der Linden, S., and Hostert, P.:
865 National-scale mapping of building height using Sentinel-1 and Sentinel-2 time series, *Remote Sens*
866 *Environ*, 252, 112128, 10.1016/j.rse.2020.112128, 2021.

867 Gacu, J. G., Monjardin, C. E. F., de Jesus, K. L. M., and Senoro, D. B.: GIS-Based Risk Assessment of
868 Structure Attributes in Flood Zones of Odiongan, Romblon, Philippines, *Buildings*, 13, 506, 2023.

869 Garvey, P. R. and Lansdowne, Z. F.: Risk matrix: an approach for identifying, assessing, and ranking
870 program risks, *Air Force Journal of Logistics*, 22, 18-21, 1998.

871 Glahn, B., Taylor, A., Kurkowski, N., and Shaffer, W. A. J. N. W. D.: The role of the SLOSH model in
872 National Weather Service storm surge forecasting, 33, 3-14, 2009.

873 Grahn, T. and Nyberg, R.: Damage assessment of lake floods: Insured damage to private property
874 during two lake floods in Sweden 2000/2001, *International journal of disaster risk reduction*, 10, 305-
875 314, 2014.

876 Granger, K.: Quantifying storm tide risk in Cairns, *Natural Hazards*, 30, 165-185, 2003.

877 Hasanzadeh Nafari, R., Ngo, T., and Lehman, W.: Calibration and validation of
878 FLFA_{rs} -- a new flood loss function for Australian residential structures,
879 *Natural Hazards and Earth System Sciences*, 16, 15-27, 10.5194/nhess-16-15-2016, 2016.

880 Hess, T. M. and Morris, J.: Estimating the value of flood alleviation on agricultural grassland,
881 *Agricultural Water Management*, 15, 141-153, 1988.

882 Holland, G. J.: An analytic model of the wind and pressure profiles in hurricanes, 1980.

883 Hu, K., Meselhe, E., Rhode, R., Snider, N., and Renfro, A.: The Impact of Levee Openings on Storm
884 Surge: A Numerical Analysis in Coastal Louisiana, *Applied Sciences*, 12, 10884, 2022.

885 Huang, H., Chen, P., Xu, X., Liu, C., Wang, J., Liu, C., Clinton, N., and Gong, P.: Estimating building
886 height in China from ALOS AW3D30, *ISPRS Journal of Photogrammetry and Remote Sensing*, 185,
887 146-157, 10.1016/j.isprsjprs.2022.01.022, 2022.

888 Huizinga, J., De Moel, H., and Szewczyk, W.: Global flood depth-damage functions: Methodology and
889 the database with guidelines, 2017.

890 Ji, S., Wei, S., and Lu, M.: Fully convolutional networks for multisource building extraction from an
891 open aerial and satellite imagery data set, *IEEE Transactions on geoscience and remote sensing*, 57,
892 574-586, 2018.

893 Ji, T., Li, G., Liu, Y., Liu, R., and Zhu, Y.: Spatiotemporal Features of Storm Surge Activity and Its
894 Response to Climate Change in the Southeastern Coastal Area of China in the Past 60 years, *Journal of*
895 *Geophysical Research: Atmospheres*, 126, 2020.

896 Kang, C. L., Cheng, Y., Wang, F., Zong, M. M., Luo, J., and Lei, J. Y.: THE APPLICATION OF UAV
897 OBLIQUE PHOTOGRAMMETRY IN SMART TOURISM: A CASE STUDY OF LONGJI
898 TERRACED SCENIC SPOT IN GUANGXI PROVINCE, *The International Archives of the*
899 *Photogrammetry, Remote Sensing and Spatial Information Sciences*, XLII-3/W10, 575-580, 2020.

900 Kreibich, H., Seifert, I., Merz, B., and Thielen, A. H.: Development of FLEMOcs – a new model for
901 the estimation of flood losses in the commercial sector, *Hydrological Sciences Journal*, 55, 1302-1314,

902 2010.

903 Kron, W.: Flood risk= hazard• values• vulnerability, *Water international*, 30, 58-68, 2005.

904 Lee, J.: The economic aftermath of Hurricanes Harvey and Irma: The role of federal aid, *International*
905 *journal of disaster risk reduction*, 61, 102301, 2021.

906 Li, X., Zhou, Y., Gong, P., Seto, K. C., and Clinton, N.: Developing a method to estimate building
907 height from Sentinel-1 data, *Remote Sensing of Environment*, 240, 10.1016/j.rse.2020.111705, 2020.

908 Liu, W.-C. and Huang, W.-C.: Investigating typhoon-induced storm surge and waves in the coast of
909 Taiwan using an integrally-coupled tide-surge-wave model, *Ocean Engineering*, 212, 107571, 2020.

910 Liu, Y., Li, Z., Wei, B., Li, X., and Fu, B.: Seismic vulnerability assessment at urban scale using data
911 mining and GIScience technology: application to Urumqi (China), *Geomatics, Natural Hazards and*
912 *Risk*, 10, 958-985, 2019.

913 Liu, Y., So, E., Li, Z., Su, G., Gross, L., Li, X., Qi, W., Yang, F., Fu, B., and Yalikun, A.: Scenario-
914 based seismic vulnerability and hazard analyses to help direct disaster risk reduction in rural Weinan,
915 China, *International Journal of Disaster Risk Reduction*, 48, 101577, 2020.

916 Lyddon, C. E., Brown, J. M., Leonardi, N., Saulter, A., and Plater, A. J.: Quantification of the
917 Uncertainty in Coastal Storm Hazard Predictions Due to Wave-Current Interaction and Wind Forcing,
918 *Geophysical Research Letters*, 46, 14576-14585, 2019.

919 Malekinezhad, H., Sepehri, M., Pham, Q. B., Hosseini, S. Z., Meshram, S. G., Vojtek, M., and
920 Vojteková, J.: Application of entropy weighting method for urban flood hazard mapping, *Acta*
921 *Geophysica*, 69, 841-854, 2021.

922 Marvi, M. T.: A review of flood damage analysis for a building structure and contents, *Natural Hazards*,
923 102, 967-995, 10.1007/s11069-020-03941-w, 2020.

924 Masson, D.: A case study of wave–current interaction in a strong tidal current, *Journal of physical*
925 *oceanography*, 26, 359-372, 1996.

926 McGranahan, G., Balk, D., and Anderson, B.: The rising tide: assessing the risks of climate change and
927 human settlements in low elevation coastal zones, *Environment and urbanization*, 19, 17-37, 2007.

928 McPherson, M.: Responding to Typhoon Haiyan in the Philippines, *Western Pacific Surveillance and*
929 *Response Journal*, 6, 1-4, 2015.

930 Merz, B., Kreibich, H., and Lall, U.: Multi-variate flood damage assessment: a tree-based data-mining
931 approach, *Natural Hazards and Earth System Sciences*, 13, 53-64, 2013.

932 Merz, B., Thieken, A. H., and Gocht, M.: Flood risk mapping at the local scale: concepts and
933 challenges, *Flood risk management in Europe: innovation in policy and practice*, 231-251, 2007.

934 Mharzi Alaoui, H., Radoine, H., Chenal, J., Hajji, H., and Yakubu, H.: Deep building footprint
935 extraction for urban risk assessment–Remote sensing and Deep learning based approach, *The*
936 *International Archives of the Photogrammetry, Remote Sensing and Spatial Information Sciences*, 48,
937 83-86, 2022.

938 Nastev, M. and Todorov, N.: Hazus: A standardized methodology for flood risk assessment in Canada,
939 *Canadian Water Resources Journal*, 38, 223-231, 2013.

940 Paprotny, D., Kreibich, H., Morales-Nápoles, O., Castellarin, A., Carisi, F., and Schröter, K.: Exposure
941 and vulnerability estimation for modelling flood losses to commercial assets in Europe, *Science of The*
942 *Total Environment*, 737, 140011, 2020.

943 Pathan, A. I., Girish Agnihotri, P., Said, S., and Patel, D.: AHP and TOPSIS based flood risk
944 assessment- a case study of the Navsari City, Gujarat, India, *Environmental Monitoring and*
945 *Assessment*, 194, 2022.

946 Rafiei-Sardooi, E., Azareh, A., Choubin, B., Mosavi, A. H., and Clague, J. J.: Evaluating urban flood
947 risk using hybrid method of TOPSIS and machine learning, *International Journal of Disaster Risk*
948 *Reduction*, 66, 102614, 2021.

949 Ramkar, P. and Yadav, S. M.: Flood risk index in data-scarce river basins using the AHP and GIS
950 approach, *Natural Hazards*, 109, 1119-1140, 2021.

951 Rizzi, J., Torresan, S., Zabeo, A., Critto, A., Tosoni, A., Tomasin, A., and Marcomini, A.: Assessing
952 storm surge risk under future sea-level rise scenarios: a case study in the North Adriatic coast, *Journal*
953 *of Coastal Conservation*, 21, 453-471, 10.1007/s11852-017-0517-5, 2017.

954 Rousell, A. and Zipf, A.: Towards a Landmark-Based Pedestrian Navigation Service Using OSM Data,
955 *ISPRS international journal of geo-information*, 6, 64, 2017.

956 Scawthorn, C., Blais, N., Seligson, H., Tate, E., Mifflin, E., Thomas, W., Murphy, J., and Jones, C.:
957 HAZUS-MH flood loss estimation methodology. I: Overview and flood hazard characterization,
958 *Natural Hazards Review*, 7, 60-71, 2006.

959 Seto, K. C., Fragkias, M., Güneralp, B., and Reilly, M. K.: A meta-analysis of global urban land
960 expansion, *PloS one*, 6, e23777, 2011.

961 Shao, Y., Taff, G. N., and Walsh, S. J.: Shadow detection and building-height estimation using
962 IKONOS data, *International Journal of Remote Sensing*, 32, 6929-6944,
963 10.1080/01431161.2010.517226, 2011.

964 Shi, X., Tan, J., Guo, Z., and Liu, Q.: A review of risk assessment of storm surge disaster, *Advances in*
965 *Earth Science*, 28, 866, 2013.

966 Smith, D. I.: Flood damage estimation - A review of urban stage-damage curves and loss functions,
967 *Water S. A.*, 20, 231-238, 1994.

968 Sutskever, I., Vinyals, O., and Le, Q. V.: Sequence to sequence learning with neural networks,
969 *Advances in neural information processing systems*, 27, 2014.

970 Tang, J., Wang, L., and Yao, Z.: Analyzing urban sprawl spatial fragmentation using multi-temporal
971 satellite images, *GIScience & Remote Sensing*, 43, 218-232, 2006.

972 Taramelli, A., Righini, M., Valentini, E., Alfieri, L., Gatti, I., and Gabellani, S.: Building-scale flood
973 loss estimation through vulnerability pattern characterization: application to an urban flood in Milan,
974 Italy, *Natural Hazards and Earth System Sciences*, 22, 3543-3569, 10.5194/nhess-22-3543-2022, 2022.

975 Tate, E., Munoz, C., and Suchan, J.: Uncertainty and sensitivity analysis of the HAZUS-MH flood
976 model, *Natural Hazards Review*, 16, 04014030, 2015.

977 Thieken, A. H., Olschewski, A., Kreibich, H., Kobsch, S., and Merz, B.: Development and evaluation
978 of FLEMOps – a new Flood Loss Estimation MOdel for the private sector, *Flood Recovery, Innovation*
979 *and Response I*, 10.2495/friar080301, 2008.

980 Vijayan, L., Huang, W., Yin, K., Ozguven, E., Burns, S., and Ghorbanzadeh, M.: Evaluation of
981 parametric wind models for more accurate modeling of storm surge: a case study of Hurricane Michael,
982 *Natural Hazards*, 106, 2003-2024, 2021.

983 Wang, N., Hou, Y., Mo, D., and Li, J.: Hazard assessment of storm surges and concomitant waves in
984 Shandong Peninsula based on long-term numerical simulations, *Ocean & Coastal Management*, 213,
985 105888, 2021a.

986 Wang, S., Mu, L., Yao, Z., Gao, J., Zhao, E., and Wang, L.: Assessing and zoning of typhoon storm
987 surge risk with a geographic information system (GIS) technique: a case study of the coastal area of
988 Huizhou, *Natural Hazards and Earth System Sciences*, 21, 439-462, 10.5194/nhess-21-439-2021,
989 2021b.

990 Wu, J., Ye, M., Wang, X., and Koks, E.: Building Asset Value Mapping in Support of Flood Risk
991 Assessments: A Case Study of Shanghai, China, 2019.

992 Yang, J., Li, L., Zhao, K., Wang, P., Wang, D., Sou, I. M., Yang, Z., Hu, J., Tang, X., Mok, K. M., and
993 Liu, P. L. F.: A Comparative Study of Typhoon Hato (2017) and Typhoon Mangkhut (2018)—Their
994 Impacts on Coastal Inundation in Macau, *Journal of Geophysical Research: Oceans*, 124, 9590-9619,
995 10.1029/2019jc015249, 2019.

996 Yang, Z., Shao, W., Ding, Y., Shi, J., and Ji, Q.: Wave Simulation by the SWAN Model and FVCOM
997 Considering the Sea-Water Level around the Zhoushan Islands, *Journal of Marine Science and
998 Engineering*, 8, 783, 2020.

999 Yazdi, J. and Salehi Neyshabouri, S. A. A.: Optimal design of flood-control multi-reservoir system on a
1000 watershed scale, *Natural hazards (Dordrecht)*, 63, 629-646, 2012.

1001 Yu: NHESS_dataset, 10.6084/m9.figshare.24586605.v2, 2023.

1002 Zhai, G., Fukuzono, T., and Ikeda, S.: MODELING FLOOD DAMAGE: CASE OF TOKAI FLOOD
1003 20001, *Journal of the American Water Resources Association*, 41, 77-92, 2005.

1004 Zhang, S., Zhang, J., Li, X., Du, X., Zhao, T., Hou, Q., and Jin, X.: Quantitative risk assessment of
1005 typhoon storm surge for multi-risk sources, *J Environ Manage*, 327, 116860,
1006 10.1016/j.jenvman.2022.116860, 2023.

1007 Zhang, Z., Chen, C., Song, Z., Zhang, D., Hu, D., and Guo, F.: A FVCOM study of the potential coastal
1008 flooding in apponagansett bay and clarks cove, Dartmouth Town (MA), *Natural Hazards*, 103, 2787-
1009 2809, 2020.

1010 Zhou, C., Chen, P., Yang, S., Zheng, F., Yu, H., Tang, J., Lu, Y., Chen, G., Lu, X., Zhang, X., and Sun,
1011 J.: The impact of Typhoon Lekima (2019) on East China: a postevent survey in Wenzhou City and
1012 Taizhou City, *Frontiers of Earth Science*, 16, 109-120, 10.1007/s11707-020-0856-7, 2021.

1013 Zhou, G., Song, C., Simmers, J., and Cheng, P.: Urban 3D GIS from LiDAR and digital aerial images,
1014 *Computers & geosciences*, 30, 345-353, 2004.

1015 Zhu, T., Ke, S., Li, W., Chen, J., Yun, Y., and Ren, H.: WRF-CFD/CSD analytical method of
1016 hydroelastic responses of ultra-large floating body on maritime airport under typhoon-wave-current
1017 coupling effect, *Ocean Engineering*, 261, 112022, 2022.

1018